nature medicine

Article

https://doi.org/10.1038/s41591-026-04354-1

Targeted therapies plus radiotherapy for diffuse intrinsic pontine glioma: the randomized phase 2 BIOMEDE trial

Received: 2 October 2025

Accepted: 18 March 2026

Published online: 24 April 2026

Check for updates

A list of authors and their affiliations appears at the end of the paper

Diffuse intrinsic pontine glioma (DIPG) is the pediatric tumor with the worst prognosis. BIOMEDE was a randomized phase 2 trial comparing the efficacy in terms of overall survival (OS) (primary endpoint) of epidermal growth factor receptor (EGFR) inhibitor erlotinib, mTOR inhibitor everolimus and multitargeted tyrosine kinase inhibitor dasatinib in combination with radiotherapy in patients with a biopsy-proven DIPG. Tumors were assessed centrally for immunohistochemical biomarkers (EGFR overexpression or PTEN loss) together with whole-exome and RNA sequencing. A cohort of 66 children with the same inclusion criteria and treated previously with temozolomide-based regimen was used to compare outcome. Treatment allocation was performed by randomization in 233 patients, designed so that a drug could not be allocated if the corresponding biomarker was absent: 36 received erlotinib, 102 received dasatinib and 95 received everolimus. The trial was ended for futility of the primary endpoint following the recommendations of the independent data monitoring committee: OS from biopsy was not different from the control cohort (median OS = 10.8 months (95% confidence interval (CI): 9.5–13.0)) in any of the three arms (median OS = 9.7 months (95% CI: 7.8–14.6) for erlotinib; 9.9 months (95% CI: 8.8–11.2) for dasatinib; and 11.9 months (95% CI: 10.7–14.2) for everolimus). Everolimus showed significantly less ocular, renal, skin and gastrointestinal side effects and treatment discontinuation for toxicity (secondary endpoint). *TP53* mutations, frequently linked to multiple structural chromosomal aberrations, were the strongest predictor for poor survival in multivariate analysis (hazard ratio = 2.8 (95% CI: 1.9–4.2), $P < 0.0001$). Both mutations in and activation of the mTOR pathway were associated with a better response to everolimus. Four long-term survivors treated with an mTOR inhibitor were alive free of treatment over 6 years from diagnosis. With comprehensive tumor profiling, BIOMEDE validated prognostic biomarkers as well as informative theranostic biomarkers for future trials. ClinicalTrials.gov: NCT02233049.

e-mail: marie-anne.debily@gustaveroussy.fr; jacques.grill@gustaveroussy.fr

DIPGs are currently incurable. Long diagnosed on clinical and radiological characteristics only, this disease is now molecularly defined by the loss of the trimethylation mark at lysine 27 of the histone H3 protein, which leads to a specific reorganization of the epigenetic landscape of the tumor cells[1]. This unique oncogenic mechanism is shared by other diffuse gliomas located in the midline outside the pons[2] and posterior fossa type A ependymoma[3,4]. This alteration is caused by the dysfunction of the PRC2 complex due to either a missense K27M mutation of the histone H3-encoding genes[5] or the overexpression of EZHIP, both interfering with EZH2 enzyme activity[6,7]. Consequently, the World Health Organization (WHO) has defined a new entity named diffuse midline glioma (DMG) H3K27-altered where DIPG refers to tumors with pontine location. Deep location and invasion preclude surgical excision. Radiotherapy is the mainstay of treatment since the first description of its efficacy[8]. Radiotherapy does not cure patients with DIPG, and families and caregivers request adjuvant therapies. No effective chemotherapy has been identified despite the completion of numerous single-arm phase 2 trials. The chemoresistance of these neoplasms has prompted efforts to study the biology of these tumors for specific targets.

In the past two decades, the reintroduction of stereotactic biopsies[9] and increased autopsy studies[10–12] have helped identifiy actionable targets, such as PDGFRA[13–15], EGFR[16,17] and mTOR[13]. Targeted therapies, including dasatinib[18], were shown to outperform conventional chemotherapy in both preclinical models and clinical trials[16,18–21].

Biopsy became useful again not only for diagnosis but also for prognostication since outcomes were reported to be associated with the type of histone H3 mutated[22].

In 2014, we launched an international randomized trial for biopsy-proven DIPG (presence of a loss of trimethylation at position K27 of histone H3 being the main inclusion criterion) in children, adolescents and young adults. This included biomarker-driven randomization among three drugs previously tested in phase 1 in patients with DIPG targeting the most frequent druggable alterations known at that time: EGFR tyrosine kinase inhibitor erlotinib, mTOR inhibitor everolimus and multitarget receptor tyrosine kinase inhibitor dasatinib. Several targets of dasatinib such as ABL, the SRC family kinases and the receptor tyrosine kinases c-KIT, platelet-derived growth factor receptor (PDGFR) α and β, discoidin domain receptor 1 (DDR1), c-FMS and ephrin receptors are overexpressed in DIPG compared to normal brainstem, and efficacy of dasatinib has been shown in vitro on DIPG cells[15,18]. These medicines were given concomitantly with radiotherapy and as adjuvant therapy until progression. OS was the primary outcome measure. All biopsies were studied with whole-exome sequencing (WES) and RNA sequencing (RNA-seq) to refine the molecular description of the different forms of the disease and to explore prognostic and theranostic biomarkers (exploratory objectives). Here we present the final results of this large trial and its biological correlates.

Results

Population of the study and control cohort

A total of 326 patients were enrolled between 2 October 2014 and 6 May 2020 (Fig. 1). Thirty-four patients were treated with everolimus after the trial steering committee's recommendation to stop randomization.

Among the 292 patients enrolled before randomization closed, 43 were screen failures. Thirteen with non-brainstem DMG (NB-DMG) H3K27-altered became eligible in the trial after the change of the WHO classification. Of these 43, 33 did not meet eligibility criteria (including 23 with a diagnosis centrally rejected), and 10 withdrew consent. Three more patients were not randomized for other reasons. The most frequent differential diagnoses were ganglioglioma, pilocytic astrocytoma, pediatric high-grade glioma of the subclass MYCN (pedHGG-MYCN), *MYB–QKI* angiocentric glioma and NF1-related glioma (Supplementary Table 1).

In total, 233 patients were randomized in the three subtrials (Table 1) until 20 September 2019 when the independent data monitoring committee recommended stopping randomization for futility (Fig. 1). Ninety-five patients were randomized to receive everolimus, 102 to receive dasatinib and 36 to receive erlotinib. Sex was balanced. Median age was 8.1 years (range, 1.8–30.3). Seventy-two percent were treated in France. Other brainstem structures than pons were involved in 43%, and 3% had metastases at diagnosis.

The median interval between radiological diagnosis and treatment initiation was 26.5 days (interquartile range (IQR), 21–32) (Supplementary Table 2).

Sixty-six patients with biopsy-proven DIPG treated in Gustave Roussy before the start of BIOMEDE[23,24] were used as historical controls, excluding those who had received any BIOMEDE drugs. Most received radiotherapy and temozolomide.

Trial design and endpoints

Patients with radiologically suspected DIPG first consented to biopsy. After diagnosis confirmation (DMG H3K27-altered with an epicenter in the pons) by central pathology reviewer, enrollment in the treatment randomization based on biomarkers was offered in case of age over 6 months, absence of active intratumoral hemorrhage, ability to undergo radiotherapy, Lansky Play Scale >50% and life expectancy longer than 3 months. Metastatic disease was allowed.

The drugs tested were administered during and after normofractionated radiotherapy at 54 Gy. Three drugs were compared: everolimus 5 mg m^{-2} per dose once daily, erlotinib 125 mg m^{-2} per dose once daily or dasatinib 85 mg m^{-2} per dose twice daily. The trial was designed to randomize these three drugs in patients with biopsy-proven DIPG according to specific biomarkers (Extended Data Fig. 1). According to the biomarker constellation present, three randomizations were possible: R1 (erlotinib versus dasatinib) in patients where tumor was EGFR positive without PTEN loss; R2 (everolimus versus dasatinib) in patients where tumor showed only PTEN loss without EGFR overexpression; and R3 (erlotinib versus everolimus versus dasatinib) in patients with tumor showing both EGFR overexpression and PTEN loss (Extended Data Fig. 1). In total, eight patients were randomized in R1, 136 in R2 and 89 in R3 (Fig. 1 and Extended Data Table 1). Patients with biomarker-negative tumors received dasatinib without randomization and were excluded from the final analysis. Patients without information on biomarkers (biopsy not diagnostic but centrally reviewed radiologic features of DIPG, necrotic tumor not amenable to immunohistochemical analysis or lack of material for biomarkers) were assigned in R3. This design enabled pairwise drug efficacy comparisons by distributing R3 patients according to a given pairwise comparison; these OS comparisons were the primary objective. Considering the smallest pairwise comparison (erlotinib versus everolimus), 79 events and 90 patients were required to achieve 80% power to compare OS curves using a two-sided log-rank test ($\alpha = 20\%$), if the hazard ratio of death was 0.62, equivalent to a 10.6% increase in the 2-year OS (5% versus 15.6%) assuming an exponential survival distribution, proportional hazards and an expected accrual of 22.5 patients per year (East software; Cytel). Considering the expected biomarker distribution, we planned to recruit a total of 250 patients in the entire randomized trial to ensure 90 patients in the smallest pairwise comparison (erlotinib versus everolimus). Comparison with historical controls was also part of this primary objective.

Secondary endpoints were 2-year OS, progression-free survival (PFS) and safety profile. The biomarkers associated with disease outcome, the association between biomarkers and drug efficacy and the radiographic changes observed after radiotherapy were the planned exploratory objectives.

Survival analysis

The trial did not show any significant OS difference (Fig. 2a–d and Extended Data Table 2). With a median follow-up of 5.3 years, median

https://doi.org/10.1038/s41591-026-04354-1

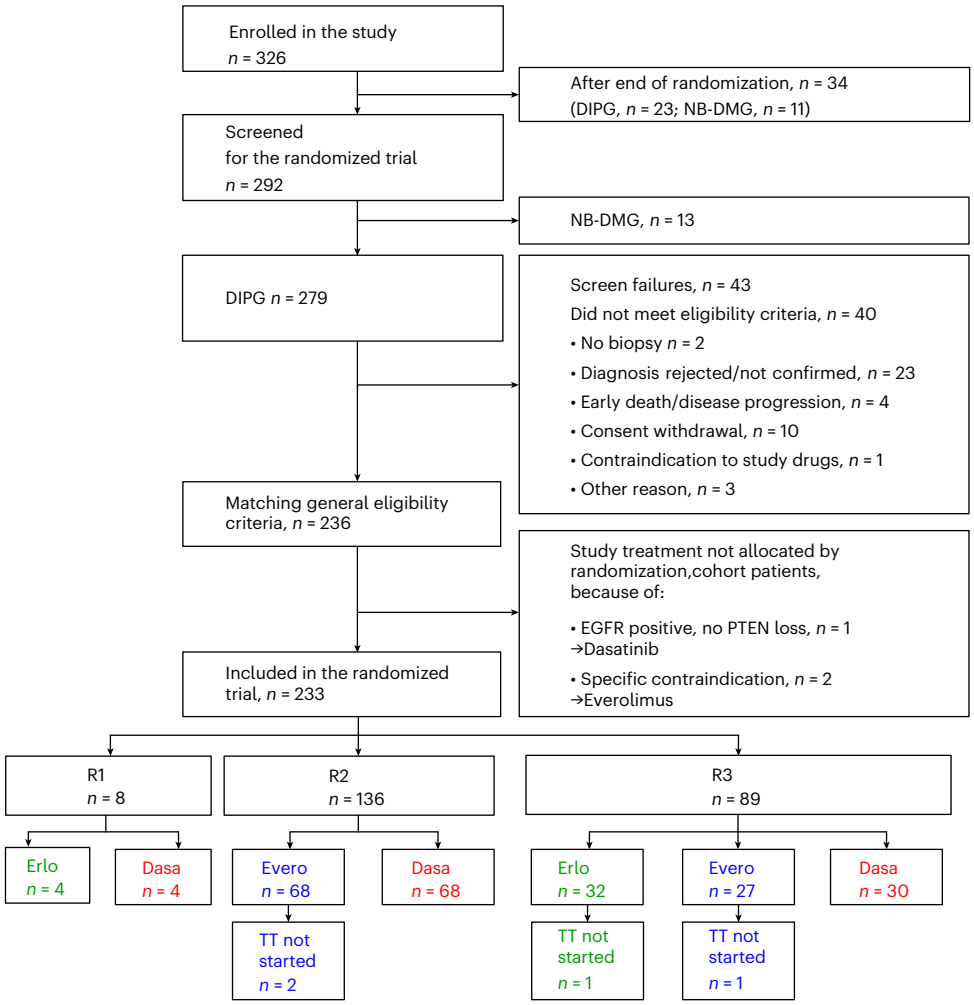

Fig. 1 | CONSORT diagram of the 326 patients enrolled in the study. Thirty-four patients were enrolled after the end of randomization (Amendment 7) and were, therefore, not included in the analysis. Thirteen patients with NB-DMG were randomized in the trial after Amendment 7, which authorized the enrollment of DMG located outside the pons, and these patients were not considered for the main analysis. Dasa, dasatinib; Erlo, erlotinib; Evero, everolimus; TT, treatment.

OS since the biopsy was 11.1 months (95% CI: 9.7–11.7) in the trial compared to 10.8 months in the control cohort (95% CI: 9.5–13.0). No difference was observed for any of the treatment arms compared to the historical control, with median OS of 9.7 months (95% CI: 7.8–14.6), 9.9 months (95% CI: 8.8–11.2) and 11.9 months (95% CI: 10.7–14.2) for patients treated with erlotinib, dasatinib and everolimus, respectively (Fig. 2e and Extended Data Table 2).

Because there was no recommendation for treatment at progression, some patients switched to the drug used in other arms, and some patients received reirradiation at the time of progression, especially if PFS was superior or equal to 6 months. We considered reirradiation as a possible confounding factor for OS analysis. The reirradiation rate was similar in the three treatment arms: 25% of patients underwent reirradiation—30% in the everolimus arm, 22% in the dasatinib arm and 22% in the erlotinib arm (Fisher's exact test, $P = 0.32$).

To allow comparison of survival with studies not mandating the biopsy as a diagnostic procedure, median OS after radiological diagnosis was measured: 10.3 months (95% CI: 8–14.8), 10.5 months (95% CI: 9.5–11.5) and 12.1 months (95% CI: 10.9–14.6) for patients randomized to erlotinib, dasatinib and everolimus, respectively.

PFS was not different in the three treatment arms (log-rank test, $P = 0.89$; Extended Data Fig. 2a).

The 2-year OS was similar in the three arms: 144 patients (62%) survived less than 1 year; 70 (30%) survived between 1 year and 2 years; and 19 (8%) survived more than 2 years (Extended Data Table 2).

Safety

Safety and outcome of the biopsy procedure. Neurosurgeons performing the biopsies were either authorized based on their previous track records for this procedure or trained in two dedicated sessions (S.P. and K.A.). No biopsy-related deaths were reported. Median hospital stay for the biopsy was 2 days (range, 1–5). In the 157 biopsy procedures that were randomly centrally reviewed, 38 patients experienced neurological worsening, of which 27 occurred within 48 hours of the biopsy and were, therefore, considered related to the procedure. Fourteen severe (grade 3–4) complications were reported, regardless of center biopsy volume.

Whatever the depth of the tumor biopsy judged centrally on postoperative computed tomography or magnetic resonance imaging (MRI), the median variant allele frequency (VAF) of the H3K27M mutation was approximately 40% (Extended Data Fig. 3a–d). Tumor mutation burden was not associated with the VAF of the histone H3K27M mutation (Extended Data Fig. 3e). Nucleic acid extraction yielded a median of 9.8 µg of DNA and 2.9 µg of RNA of sufficient quality (that is, RNA integrity number (RIN) > 5), enabling subsequent genomic analyses in 176 cases.

Treatment-related adverse events. Treatments were well tolerated. No patient died from study treatment-related complications. Seventy-eight percent of patients experienced grade 3 or grade 4 adverse events during treatment. When considering adverse

https://doi.org/10.1038/s41591-026-04354-1

Table 1 | Patient and disease characteristics, overall and by treatment group allocated by randomization (*n*=233)

Characteristics	Erlotinib *n*=36		Everolimus *n*=95		Dasatinib *n*=102		Total *n*=233	
	n	%	*n*	%	*n*	%	*n*	%
Country								
France	23	63.9	70	73.7	75	73.5	168	72.1
UK	7	19.4	15	15.8	14	13.7	36	15.5
The Netherlands	0	0	0	0	1	1.0	1	0.4
Spain	1	2.8	0	0	2	2.0	3	1.3
Denmark	1	2.8	4	4.2	7	6.9	12	5.2
Sweden	3	8.3	3	3.2	1	1.0	7	3.0
Australia	1	2.8	2	2.1	2	2.0	5	2.2
New Zealand	0	0	1	1.1	0	0	1	0.4
Age at study entry (years)								
Median	9.5		7.8		8.1		8.1	
Q1–Q3	5.4–11.9		5.8–9.7		5.4–12.5		5.7–11.4	
Min–Max	2.6–20.9		1.9–25.9		1.8–30.3		1.8–30.3	
<5 years	6	16.7	15	15.8	21	20.6	42	18.0
5–10 years	16	44.4	57	60.0	44	43.1	117	50.2
≥10 years	14	38.9	23	24.2	37	36.3	74	31.8
Sex								
Male	19	52.8	43	45.3	52	51.0	114	48.9
Female	17	47.2	52	54.7	50	49.0	119	51.1
Histone mutation								
Wild-type	6	16.7	11	11.6	5	4.9	22	9.4
H3.1 K27M	3	8.3	10	10.5	16	16.0	29	12.5
H3.3 K27M	18	50.0	56	58.9	67	65.7	141	60.5
NA	9	25.0	18	19.0	14	13.7	41	17.6
PTEN status								
PTEN loss	24	66.7	79	83.2	81	79.4	184	78.9
PTEN positive/no PTEN loss	4	11.1	0	0	4	3.9	8	3.4
PTEN unknown	8	22.2	16	16.8	17	16.7	41	17.6
EGFR status								
Overexpression	31	86.1	24	25.3	30	29.4	85	36.5
EGFR negative	0	0	68	71.6	68	66.7	136	58.4
EGFR unknown	5	13.9	3	3.2	4	3.9	12	5.2
TP53 mutation								
No	10	27.8	36	37.9	30	29.4	76	32.6
Yes	14	38.9	36	37.9	55	53.9	105	45.1
Unknown	12	33.3	23	24.2	17	16.7	52	22.3
Site of primary tumor (NA=1)								
Only pontine	12	34.3	50	52.6	70	68.6	132	56.9
Brain stem but not only pontine	23	65.7	45	47.4	32	31.4	100	43.1
Metastases at study entry								
No	33	91.7	93	97.9	99	97.1	225	96.6
Yes	3	8.3	2	2.1	3	2.9	8	3.4
Randomized subtrial								
R1	4	11.1			4	3.9	8	3.4
R2			68	71.6	68	66.7	136	58.4
R3	32	88.9	27	28.4	30	29.4	89	38.2

NA, non available.

events of any grade, eye ($P < 0.0001$), skin ($P = 0.004$) and infectious ($P = 0.042$) adverse events were more frequent with erlotinib, whereas metabolic adverse events were more frequent with everolimus ($P = 0.0003$) (Extended Data Fig. 3f,g, Extended Data Table 3 and Supplementary Table 3). Severe (grade 3 or higher) skin adverse events were significantly more frequent with erlotinib ($P < 0.0001$), and severe renal ($P = 0.0054$) and gastrointestinal ($P = 0.038$) adverse events were significantly more frequent with dasatinib. Irrespective of the imputability to the treatment or the disease, neurological severe adverse events reported did not differ in their frequency among treatment arms (Fisher's exact test, $P = 0.65$) (Supplementary Table 3); the three most frequent were headaches, hydrocephalus and dizziness. Treatment was stopped because of toxicity in 20%, 3% and 14% for erlotinib, everolimus and dasatinib, respectively (Fisher's exact test, $P = 0.004$). The tolerance of everolimus was better than reported in breast cancer trials[25] and similar to a recent report in children with low-grade gliomas[26].

Exploratory outcomes

Response to therapy. Clinical improvement any time during first-line treatment was reported in 75% of the patients, whereas the clinical status was stable in 19% and deteriorated in 6%. Clinical response did not differ among treatment arms (Supplementary Table 4). Mean duration of improvement was 3.4 months, with no difference between arms. The OS of the patients with clinical improvement (11.2 months (95% CI: 10.3–12.3)) did not differ from the one of the 44 patients remaining clinically stable (9.2 months (95% CI: 6.4–10.9)) (log-rank test).

Radiologic improvement as reported by the treating physician during first-line treatment was observed in 121 patients (54%), whereas the disease remained stable as best response in 70 patients (31%) or progressed in 32 patients (14%) with no difference among treatment arms (χ^2 test, $P = 0.402$).

Pseudoprogression was reported in 110 of 233 patients (49%) with no significant difference among arms (χ^2 test, $P = 0.870$).

Planned prognostic factor analysis. *TP53* mutation was the main prognostic factor for OS and remained significant in multivariable analysis (hazard ratio = 2.84 (95% CI: 1.92–4.20), $P < 0.0001$) when adjusting for immunohistochemical biomarker status, treatment allocation, type of histone H3 alteration and age (Supplementary Tables 5 and 6 and Extended Data Fig. 4). We observed a borderline significant association between histone mutation and OS in univariate analysis ($P = 0.064$); compared to H3 wild-type (H3-WT), the outcome was worse in patients with H3.3K27M (hazard ratio = 1.28 (95% CI: 0.81–2.03)) and better in patients with H3.1K27M (hazard ratio = 0.81 (95% CI: 0.46–1.42)). *TP53* mutations were significantly more frequent in H3.3K27M than in H3.1K27M or H3-WT (67.9%, 24.1% and 28.6%, respectively; $P < 0.0001$; Supplementary Table 6), and the prognostic value of histone mutation disappeared when adjusting on covariables, in particular *TP53* mutation ($P = 0.49$ in multivariable analysis) (Extended Data Fig. 2c). Of note, as previously published[27–31], age was significantly associated in univariate analysis with OS ($P = 0.009$), with, compared to patients 10 years or older, a longer OS for the youngest (hazard ratio = 0.79 (95% CI: 0.53–1.16)) and a shorter OS for patients between 5 years and 10 years of age (hazard ratio = 1.34 (95% CI: 0.99–1.80)) (Extended Data Fig. 2d). However, H3.3K27M and *TP53* mutations were much less frequent in younger patients (Supplementary Table 7), and, when controlling for biological features of the tumor, the effect of young age appeared significantly reversed (hazard ratio = 1.72 (95% CI: 1.04–2.86)).

A planned exploratory analysis assessed clinical and known prognostic biomarkers associated with response to everolimus versus dasatinib, the only comparison with sufficient patient numbers; treatment effect appears relatively homogeneous across main subgroups (Extended Data Fig. 4).

Overall portrait of recurrent single-nucleotide variants

Mutation rates varied among patients, independently of H3 mutational status or OS (Fig. 3a). The number and type of non-synonymous coding variants were consistent with previous reports, with a median of 17.5 mutations per exome[29,30]. Missense variants accounted for most single-nucleotide variants (SNVs) (Fig. 3a).

We found predicted pathogenic germline variants in 103 patients. As recently published[31], we found recurrent alterations in *PTCH1* ($n = 3$) and in homologous recombination genes—that is, *PALPB2* ($n = 1$), *BRCA2* ($n = 2$), *BRCA1* ($n = 1$) and *CHEK2* ($n = 1$). Recurrent pathogenic germline mutations not previously reported were detected in calcium channel genes for 15.7% of patients: *RYR2* ($n = 8$), *RYR1* ($n = 5$), *RYR3* ($n = 4$), *CACNA1G* ($n = 4$), *CFTR* ($n = 4$) and *ITPR3* ($n = 5$) (Extended Data Fig. 5a).

Analysis of this large cohort refined the frequency of SNVs in DIPG (Fig. 3a). In total, 133 tumors (77%) harbored H3.3-K27M, including 89 with *TP53* mutations. Twenty-nine patients (17%) had H3.1-K27M (27 *H3C2*-mutated and two *H3C3*-mutated), of whom 19 carried *ACVR1* mutations and seven carried *TP53* mutations. Ten tumors (6%) were H3-WT after sequencing (Supplementary Table 8).

The five most frequently mutated genes, in addition to H3 genes—*TP53* (57%), *ACVR1* (17%), *ATRX* (13%), *PPM1D* (11%) and *ASXL1* (9%)—showed an average VAF higher than 35%, without being associated with frequent chromosomal gain, suggesting early events during oncogenesis (Fig. 3b and Extended Data Fig. 5b). A similar observation was made for *CDKN2C*, *ZEB2*, *PTPN11*, *PTEN*, *F8* and *ATM* although in few patients (≤6) only. By contrast, high *PDGFRA* mutation VAF was associated with gain/amplification in three of six patients, as previously reported[14].

SNVs were evenly distributed across OS groups, except for a significant enrichment of H3.3-K27M and *TP53* mutations and, to a lesser extent, *MYC* gain in patients with an OS less than 1 year ($n = 107$, 'short survivor' subgroup) (Fig. 3c). *NF1* alterations were restricted to this group.

PIK3CA (18%) and *PIK3R1* (9%) were the most frequent secondary events, with lower VAFs (Fig. 3b). *PIK3R1* alterations were found in both

Fig. 2 | Main outcome measures of the trial. The main outcome measures of the trial were based on pairwise comparisons of OS between treatment groups allocated by randomization. For these comparisons, all randomized patients were included, including those who did not start the treatment allocated by randomization (intention-to-treat analysis). OS was estimated using the Kaplan–Meier method, from the date of randomization to the date of death from any cause. **a**, OS curves: erlotinib versus dasatinib. This comparison includes 70 patients from the R1 subtrial and a subset of patients from the R3 subtrial. Median OS was 9.0 months (95% CI: 7.4–14.4) for erlotinib and 8.5 months (95% CI: 5.7–10.7) for dasatinib. The hazard ratio (HR) stratified by PTEN status was $HR_{(erlotinib/dasatinib)} = 0.87$ (95% CI: 0.52–1.46), $P = 0.59$. **b**, OS curves: everolimus versus erlotinib. This comparison includes 59 patients from the R3 subtrial. Median OS was 10.2 months (95% CI: 7.3–14.8) for erlotinib and 10.5 months (95% CI: 7.6–12.3) for everolimus. The HR stratified by EGFR status and PTEN status was $HR_{(erlotinib/everolimus)} = 0.94$ (95% CI: 0.54–1.65), $P = 0.84$. **c**, OS curves: everolimus versus dasatinib. This comparison includes 193 patients from the R2 subtrial and a subset of patients from the R3 subtrial. Median OS was 11.3 months (95% CI: 10.3–13.4) for everolimus and 9.4 months (95% CI: 8.2–10.8) for dasatinib. The HR stratified by EGFR status was $HR_{(everolimus/dasatinib)} = 0.89$ (95% CI: 0.66–1.19), $P = 0.42$. **d**, PFS in patients treated with everolimus or dasatinib. This comparison includes 193 patients from the R2 subtrial and a subset of patients from the R3 subtrial. Median PFS was 6.4 and 7.1 months, respectively. No significant difference was observed. **e**, OS since the biopsy in the three treatment arms compared to the historical control. With a median follow-up of 5.3 years, the median OS from the time of biopsy was 11.1 months (95% CI: 9.7–11.7) in the trial cohort compared to 10.8 months (95% CI: 9.5–13.0) in the historical control cohort. No significant difference was observed between any of the treatment arms and the historical control, with median OS of 9.7 months (95% CI: 7.8–14.6), 9.9 months (95% CI: 8.8–11.2) and 11.9 months (95% CI: 10.7–14.2) for patients treated with erlotinib, dasatinib and everolimus, respectively.

https://doi.org/10.1038/s41591-026-04354-1

H3.3-K27M and H3.1-K27M cases, with significant co-occurrence with *ACVR1* alteration (Extended Data Fig. 5c). *PIK3CA* alterations occurred across all OS groups, as previously described[32], with mutual exclusivity ($P < 0.01$) with H3.3-K27M. H3.1-K27M was more frequent in younger patients, whereas *TP53* mutation and *MYC* gain were enriched in older patients (Extended Data Fig. 5d,e).

First, using unbiased pathway analysis for genes mutated in more than three patients ($n = 92$), we found significant enrichment of processes related to tube morphogenesis (adjusted $P = 8.158 \times 10^{-10}$) and cell adhesion (adjusted $P = 9.06 \times 10^{-7}$). Next, analysis of frequently altered DMG pathways and functions (Extended Data Fig. 5f) showed that 170 of 172 tumors (98.8%) harbored mutations or copy number

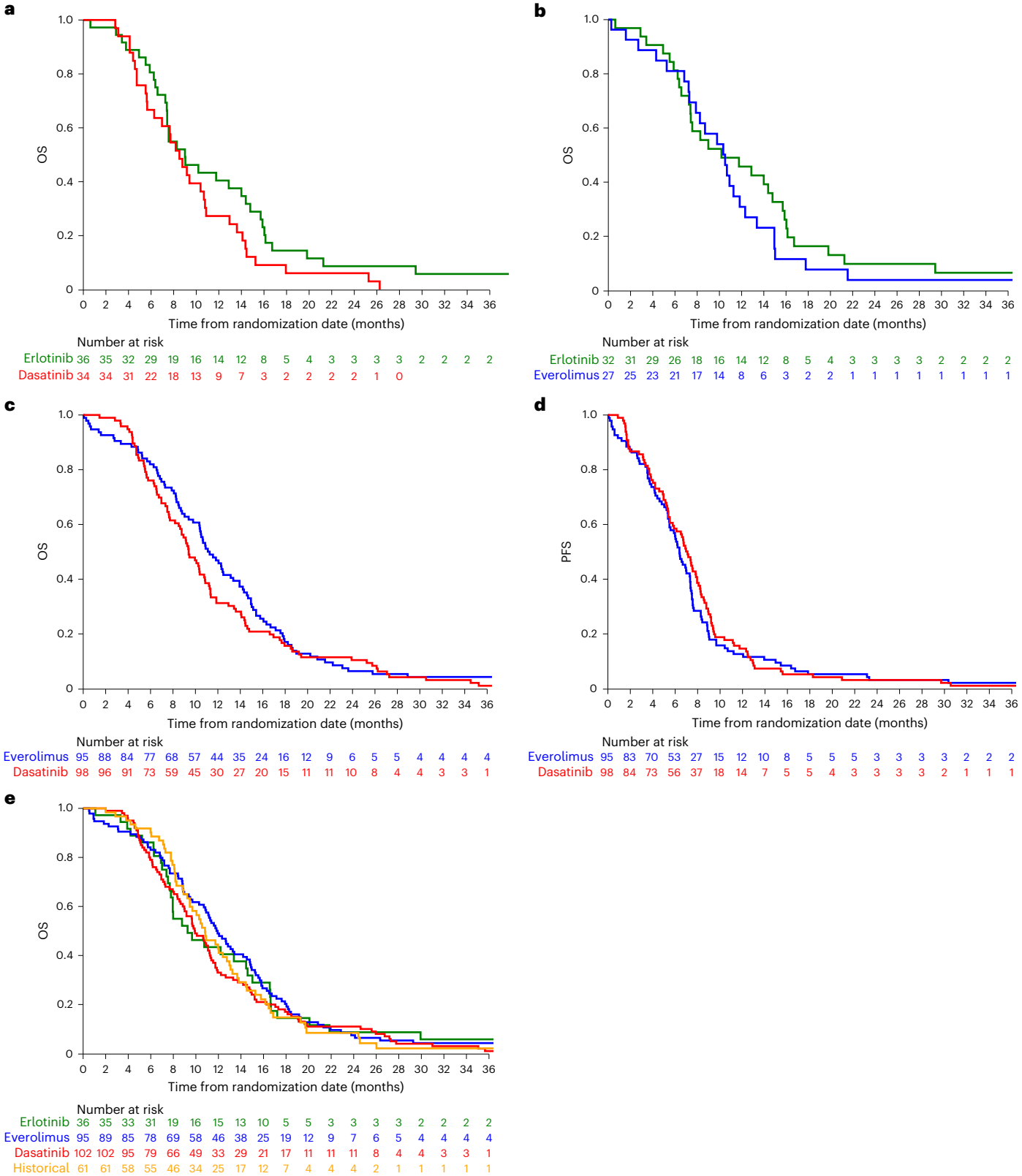

variations (CNVs) in at least one of the following seven of them: RTK/MAPK, PI3K/MTOR, TGFB signaling, genome integrity, chromatin regulators, protein homeostasis and transcription factors.

Single-base substitution (SBS) signatures analysis revealed SBS1 (deamination of 5-methylcytosine), SBS6 and SBS15 (defective DNA mismatch repair) and SBS87 (thiopurine chemotherapy exposure) as the most prevalent (Extended Data Fig. 5g,h). This profile differed from previous reports based on smaller selected subsets of tumors[33,34].

DIPG somatic copy number alteration landscape is associated with *TP53* mutation

When analyzing genome-wide copy number alterations (CNAs), we observed marked and previously unreported heterogeneity among patients with DIPG. This included frequent whole chromosome arm losses (chr14 and chr16) associated with complex genomic rearrangements across the genome or whole chromosome arm gains (chr1q and chr2) usually associated with fewer structural alterations (Supplementary Fig. 1). Ranking samples by the number of CNV segments emphasizes that widespread complex rearrangements are more common in tumors harboring *TP53* mutations (Fig. 3d, Extended Data Fig. 6b and Supplementary Fig. 1).

Copy number signature analysis highlighted a strong enrichment of CN9 in *TP53*-mutated tumors (Extended Data Fig. 6b,c). CN9 has been linked in pan-cancer analyses to poor survival and to *TP53* mutations[35]. CN12 and CN13 were also enriched in *TP53*-mutant tumors but occurred in few patients ($n = 21$ and $n = 15$, respectively) and were positively associated with *MYC* gain (Extended Data Fig. 6d). CN9 and CN12 show prominent focal loss-of-heterozygosity (LOH) patterns suggestive of structural chromosome instability (CIN)[35], whereas CN13 arises from cancers with LOH affecting over 70% of the genome, with whole-arm-scale or whole-chromosome-scale LOH events. CN9 correlates positively with chromothripsis state score, whereas the 'diploid' signatures CN1 and CN19 were negatively correlated with *TP53* mutations and positively with chr1q gain (Extended Data Fig. 6c,d).

TP53 pathway alteration is not limited to dominant-negative missense mutations

Most somatic *TP53* mutations affected the DNA-binding domain, mainly hotspot missense mutations, usually associated with a dominant-negative effect[36] (Extended Data Fig. 6e). Overall, 37% of patients harbored LOH associated with a point mutation or indel and 5.8% with compound heterozygous mutations, and 2.3% carried subclonal compound heterozygous mutations. Eleven patients had a truncating exon-6 mutation in *PPM1D*, known to mimic TP53 deficiency in the DNA damage response[37] (Supplementary Fig. 1 and Extended Data Fig. 6f,g). Twenty-five patients exhibited copy number loss of *TP53BP1*, a DNA double-strand break sensor involved in non-homologous end joining (NHEJ) DNA repair[38,39]. This loss, affecting a large portion of the chr15 arm (median 60%), was associated with significantly reduced expression of this gene ($P < 0.05$) and may impair TP53 function. The number of segments detected increases gradually with TP53 dysfunction. Tumors with *TP53* alterations had a significantly higher proportion of genome altered than $TP53^{WT}$ tumors. $TP53^{MUT}$ and $TP53^{WT}$ tumors had a median proportion of genome altered of 26% and 13%, respectively (Fig. 3e). Finally, H3.3-K27M/*TP53*-mutant tumors displayed increased segment numbers and oscillations, consistent with chromothripsis (Fig. 3d and Extended Data Fig. 6f,g).

TP53 mutations were early events in DIPG with high VAF (median 0.75 (75% CI: 0.56–0.87); Fig. 3b) and were associated with *MYC* gain (31.3% versus 9.5%, χ^2 test, $P = 6.88 \times 10^{-4}$) but were rare in tumors with chr1q gain or concomitant chr1q and chr2 gains (χ^2 test, $P = 2.83 \times 10^{-12}$ and $P = 2.79 \times 10^{-11}$, respectively) (Fig. 3f).

TP53-mutant tumors more frequently harbored *PTEN*, *SOX10* and *F8* mutations, whereas *ATM* mutations predominated in $TP53^{WT}$ (Extended Data Fig. 6j).

TP53 mutations were associated with poor OS and characteristics of aggressiveness at transcriptional level

Median OS of patients with *TP53*-mutated tumors was 8 months compared to 15 months in patients with *TP53*-wild-type tumors (Fig. 3g).

RNA-seq revealed marked upregulation of genes involved in cell cycle regulation (Benjamini–Hochberg false discovery rate (FDR) $P = 2.43 \times 10^{-11}$), chromosome segregation (Benjamini–Hochberg FDR $P = 4.47 \times 10^{-16}$) and DNA repair (Benjamini–Hochberg FDR $P = 3.14 \times 10^{-13}$) in $TP53^{MUT}$ tumors, alongside downregulation of genes involved in neuron ensheathment (Benjamini–Hochberg FDR $P = 6.06 \times 10^{-4}$) and glial cell development (Benjamini–Hochberg FDR $P = 1.1 \times 10^{-3}$) (Extended Data Fig. 6k). Additionally, oligodendrocyte markers and ectoderm development genes were repressed in *TP53*-mutant tumors. Transcriptional profiling revealed a shift toward a more immunosuppressive phenotype in *TP53*-mutant tumors. Notably, *KLRC1*, the most upregulated gene, encodes the natural killer cell

Fig. 3 | DIPG mutational landscape. a, Oncoplot depicting the most frequent somatically mutated genes in DIPG ($n = 172$), sorted in decreasing order of mutation frequency and stratified by OS—that is, less than 1 year (short), between 1 year and 2 years (intermediate) and more than 2 years (long). Twenty-two genes mutated in at least 3% of patients are shown, with mutation frequencies displayed as a bar plot on the right. Only somatic SNVs supported by more than five reads associated and with a VAF higher than 5% are shown. A stacked bar plot representing the number and types of variants per sample is displayed on the right. Germline variants supported by more than five reads and with a VAF exceeding 40% are indicated by small squares. Clinicopathological (EGFR overexpression by immunohistochemistry) and molecular annotations are displayed as bars at the top, according to the color code provided below the Oncoplot. Indels were overall rare although enriched in some genes compared to other tumor types, such as *FBXO41* and *PIK3R1*. Some genes showed frequent stop-gain mutations (*ASXL1* and *PPM1D*) or frameshift variants (*KAZN*). At the bottom, a bar plot shows, for each patient, the proportion of the 15 most prevalent COSMIC SNV signatures in the cohort after removal of 'artifactual' signatures. Patients in the 'short survivor' group exhibited mutational signature profiles associated with SBS14 (concurrent polymerase epsilon mutation and defective DNA mismatch repair), SBS18 (reactive oxygen species), SBS30 (defective base excision repair) and SBS44 (defective DNA mismatch repair) and with signatures of unknown etiology (SBS33, SBS34 and SBS39). Only SBS19 (unknown etiology) was enriched in the 'long survivor' group. **b**, Distribution of VAFs for the more frequently mutated genes. The number of patients harboring an alteration is indicated on the left; each dot represents one SNV. Whiskers indicate the minimum and maximum values within 1.5× IQR. Whiskers represent the minimum and maximum values within 1.5× IQR. Q1, Q2 and Q3 correspond to the 25th, 50th (median) and 75th percentiles, respectively. **c**, Distribution of H3-K27M, *TP53* and *PIK3CA* alterations, *MYC* gain and EGFR overexpression across survival subgroups is shown. Two-sided Fisher's exact test, $^{****}P < 0.0001$, $^{***}P < 0.001$, $^{**}P < 0.01$, $^{*}P < 0.1$; that is, $P = 0.01$ for H3-K27M, $P = 1.6 \times 10^{-7}$ for *TP53*, $P = 0.08$ for *PIK3CA* and $P = 0.001$ for *MYC* gain. **d**,**e**, Box plots showing the distribution of the percentage of altered genome number of segments and detected by CNV analysis of WES data according to *TP53* mutational status. ($TP53^{WT}$, $n = 73$, $TP53^{MUT}$, $n = 99$). The value (number of segments +1) is plotted on a $\log_{10}$ scale. Wilcoxon test, $^{*}P < 0.05$, $^{**}P < 0.01$, $^{***}P < 0.001$ and $^{****}P < 0.00001$, and $P = 1.013 \times 10^{-5}$ (**d**) and $P = 1.9 \times 10^{-10}$ (**e**). Whiskers represent the minimum and maximum values within 1.5× IQR. Q1, Q2 and Q3 correspond to the 25th, 50th (median) and 75th percentiles, respectively. **f**, Distribution of clinicopathological and molecular features shown in **a** in *TP53*-mutated and *TP53*-wild-type subgroups. Two-sided Fisher's exact test, $^{****}P < 0.0001$, $^{***}P < 0.001$, $^{**}P < 0.01$ and $^{*}P < 0.1$; that is, $P = 2.6 \times 10^{-5}$ for H3 status, $P = 9.3 \times 10^{-5}$ for *PPM1D* mutation, $P = 1.7 \times 10^{-7}$ for *ACVR1* mutation, $P = 6.9 \times 10^{-4}$ for *MYC* gain, $P = 0.01$ for *PIK3CA* mutation, $P = 1.6 \times 10^{-7}$ for survival, $P = 2.8 \times 10^{-12}$ for chr1q gain, $P = 0.07$ for chr2 gain and $P = 2.7 \times 10^{-11}$ for chr1q and chr2 gain. **g**, OS from the date of randomization in patients with $TP53^{MUT}$ and $TP53^{WT}$ DIPG ($P = 1.25 \times 10^{-8}$, two-sided log-rank test).

https://doi.org/10.1038/s41591-026-04354-1

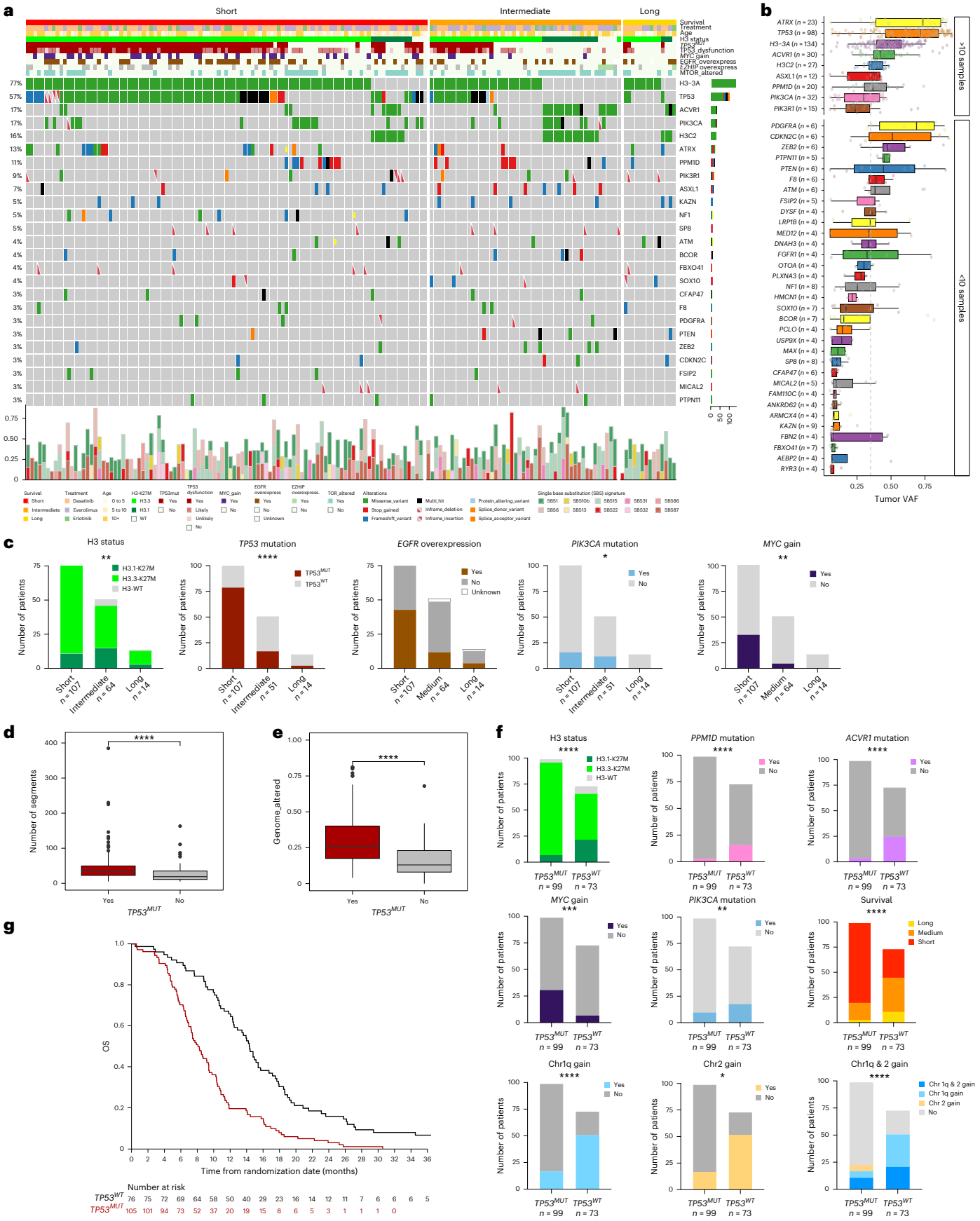

https://doi.org/10.1038/s41591-026-04354-1

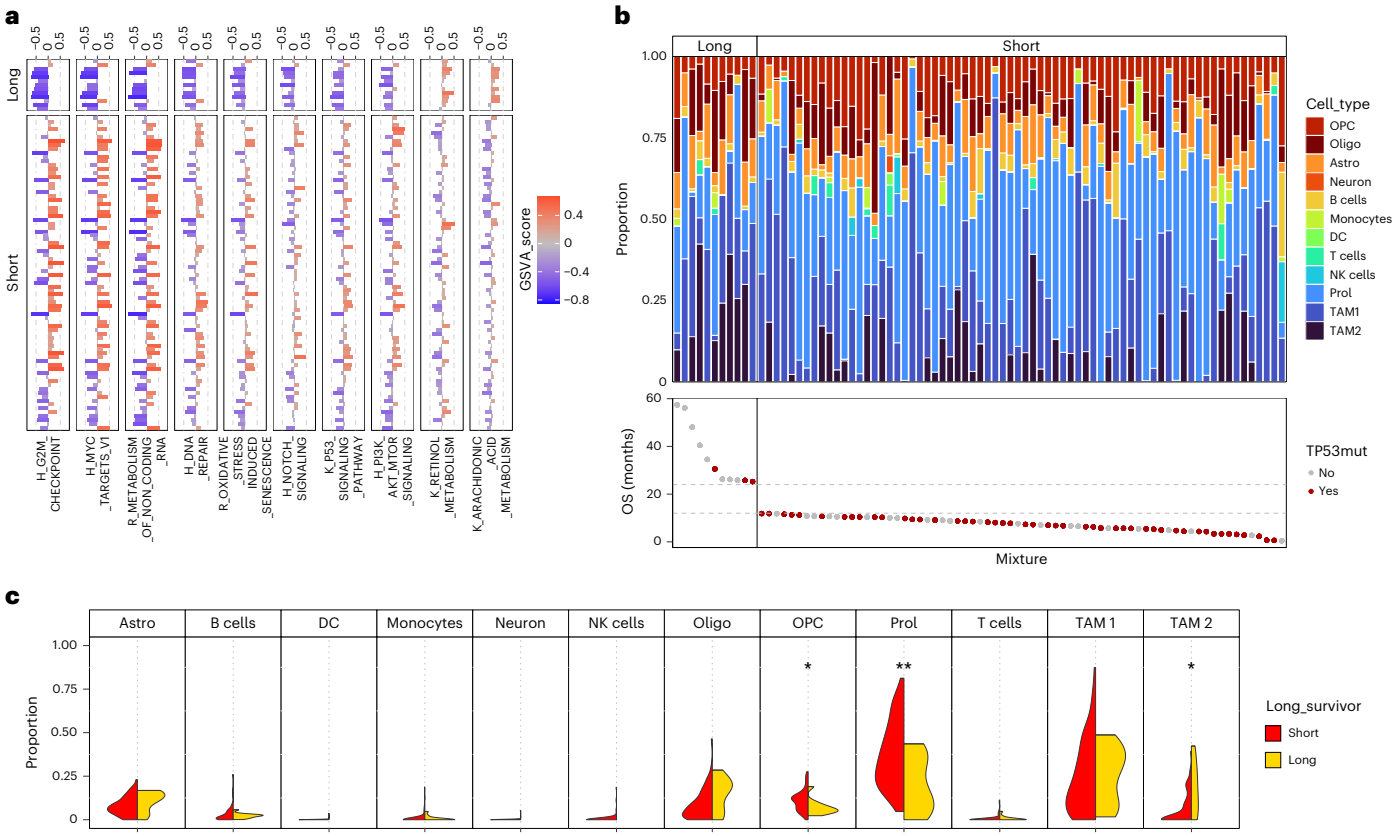

Fig. 4 | Molecular portrait of long-term survivors. a, Pathways showing significant modulation of GSVA scores between long and short survivor groups. **b**, Cell type composition of DIPG tumors inferred from deconvolution of bulk RNA-seq data (upper panel). The proportion of each cell type is indicated by a color code. OS (in months) is shown as a dot plot in the lower panel. **c**, Violin plot showing tumor cell type composition in short and long OS subgroups. Two-sided *t*-test, Holm–Bonferroni-adjusted *P* values: $^{*}P < 0.05$, $^{**}P < 0.01$; $P = 0.024$ for OPC; $P = 0.29$ for TAM2 and $P = 0.008$ for Prol. DC, dendritic cell; NK, natural killer; OPC, oligodendrocyte progenitor cell; Prol, proliferative TAM; TAM1, monocyte-derived TAM; TAM2, microglia-derived TAM.

inhibitory receptor NKG2A, a key natural killer cell immune checkpoint, inhibiting the killing ability of $CD8^{+}$ T cells. NKG2A specifically binds the non-classical human leukocyte antigen (HLA) class I molecule HLA-E, thereby transmitting inhibitory signals that impair natural killer cell function[40].

We observed marked downregulation of the long non-coding RNA *GATA2-AS1* in $TP53^{MUT}$ tumors (fold change = 0.46, adjusted $P = 2.08 \times 10^{-5}$), an MYC target, that represses *GATA2* expression and limits tumor aggressiveness[41–43]. By contrast, *TP53*-mutant tumors showed upregulation of the MET protooncogene, which promotes the proliferation, invasion and poor prognosis[44] in glioblastoma (GBM) and is amplified in a subset of DIPG[14].

Description of the four very-long-term survivors still alive 6 years from diagnosis

Four patients were alive at last follow-up, 6 years or more after diagnosis, without meaningful sequelae. Three showed residual MRI abnormalities at the last evaluation, whereas one achieved complete remission with clearance of all TP53-mutant fluid-attenuated inversion recovery (FLAIR) hypersignals (Extended Data Fig. 7a). All patients had been off treatment for at least 1 year and were treated with an mTOR inhibitor: two received everolimus and two received sirolimus due to toxicity or initial progression. No shared alterations except H3-K27M were found. One patient harbored a clonal *IDH1* R132C mutation. Two additional patients in the trial cohort (1.16%) with both *IDH1* R132C and H3.3 K27M mutations survived more than 2 years: one not randomized and treated with everolimus was alive at the last follow-up, and one treated with dasatinib died after 2.19 years.

Gene expression profile of 13 long-term survivors

We compared transcriptional profiles of 13 long-term survivors with those of 82 short-term survivors. RNA-seq revealed significant downregulation of genes involved in cell cycle regulation and chromosome segregation in long-term survivors, along with upregulation of genes involved in mitochondrial electron transport and oxidative phosphorylation (Supplementary Fig. 2 and Extended Data Fig. 7b,c).

The top 10 most downregulated genes in long-term survivors were *CENPE*, *E2F7*, *GPR139*, *IL5RA*, *NTS*, *NLRP11*, *POLQ*, *SLC7A3*, *CLS2A3P1* and *UPS32P2*. E2F7 promotes tumorigenesis via EZH2 activating the PTEN/AKT/mTOR pathway[45,46]. In DMG, E2F7 and EZH2 expression were positively correlated and elevated in short-survival patients (Extended Data Fig. 7d), and several E2F7 targets ($n = 24$, adjusted $P < 0.01$) were reduced in long-term survivors (Supplementary Fig. 2a). By contrast, the most upregulated genes in long-term survivors were *BCYRN1*, *CARD11*, *CHRM5*, *HYAL1*, *IFI27L2*, *ITPK1*, *MRO*, *PDXK* and *TNFSF12*.

We next analyzed signaling pathways by computing individual gene set variation analysis (GSVA) scores for Hallmark gene sets from the Molecular Signatures Database (MSigDB) and identified those significantly modulated between patients with long versus short OS, selecting one representative pathway per biological process (Fig. 4a). Long-term survivors showed inhibition of pathways related to DNA repair, G2/M checkpoints, MYC targets, Notch signaling, oxidative stress-induced senescence and TP53 signaling. Genes involved in PI3K/AKT/MTOR signaling were also significantly downregulated in patients with long OS. SNVs in this pathway were present across all survival subgroups. However, long-term survivors harbored no

alteration in *PI3KCA* or *NF1*, showing only in-frame deletion of *PIK3R1* (Extended Data Fig. 4a). None of the long-term survivors with RNA-seq data showed activation of the MAPK pathway nor a *BRAF* V600E or *FGFR1* mutation.

Patients with DIPG surviving longer have a distinct tumor immune microenvironment

Several differentially expressed genes according to survival supported differences in the tumor microenvironment (TME). TNFSF12, secreted by microglia-derived tumor-associated macrophages (TAMs), was significantly upregulated in long-term survivors (Supplementary Fig. 2a and Extended Data Fig. 7c)[47]; the TNFSF12–TNFRSF12A axis has been implicated in glioma progression and microglial activation in adult GBM. As previously reported, DMGs show myeloid infiltration[48]. Deconvolution of bulk RNA-seq data revealed mixed TAM ontogeny in DIPG with enrichment of microglial TAMs (Mg-TAMs) in long-term survivors, whereas monocyte-derived TAMs (Mo-TAMs), proliferative TAMs and oligodendrocyte progenitor cells were enriched in short-term survivors; overall myeloid infiltration was not associated with survival (Fig. 4b,c). Expression of the immunosuppressive cytokines *KLF2* and *TGFB1* tended to be reduced in long-term survivors (fold change adjusted $P = 0.04$ and fold change adjusted $P = 0.01$, respectively). Patients with a prolonged survival also showed higher proportions of cells with a 'myeloid cell proliferation' signature from Andrade et al.[48] as well as elevated resting CD4/CD8 T cell and CD4 naive central memory resting T cell signatures (Fig. 4c). Finally, *HOXA7* was strongly downregulated in long-term survivors; its overexpression correlates with TAM infiltration in The Cancer Genome Atlas (TCGA) and in esophageal squamous cell carcinoma (ESCC) samples[49].

Correlation between response to the treatments and clinical characteristics or biomarkers

The protocol included an exploratory analysis for efficacy biomarkers for each of the three drugs. This analysis was restricted to patients randomized to everolimus or dasatinib, as too few patients received erlotinib. The prespecified biomarkers did not influence the response to everolimus and dasatinib (Extended Data Fig. 4b,c). In addition to GSEA Hallmark PI3K/AKT/MTOR signaling, we considered alterations in a curated list of PI3K/AKT/MTOR pathway genes (Supplementary Table 9) and chr1q gain. Forest plots (Fig. 5a,b) showed association between biomarkers and treatment response (significance threshold $P < 0.1$). Chr1q gain was associated with improved PFS ($P = 0.05$) and OS ($P = 0.035$) with everolimus (Extended Data Fig. 4d–g). Similarly, mutations in PI3K/AKT/MTOR pathway correlated with better PFS ($P = 0.02$) and OS ($P = 0.08$) in everolimus-treated patients (Fig. 5c–f). Overexpression of the PI3K/AKT/MTOR signature showed a trend toward improved response to everolimus (interaction $P = 0.1085$). *PIK3CA* alterations were enriched in patients with high GSVA score for mTOR pathway expression (Fig. 5g and Extended Data Fig. 4g).

For external validation, we analyzed an independent cohort of 19 patients with biologically documented DIPG treated with an MTOR inhibitor either before BIOMEDE initiation or after the completion of randomization. Patients with overexpression of the PI3K/AKT/MTOR signature had a better OS and PFS (Extended Data Fig. 4h,i).

Discussion

To our knowledge, this study represents the largest randomized, biology-driven phase 2 trial conducted in patients with DIPG. A radiotherapy-only control arm was deemed unethical; as parent associations considered the poor outcome with radiotherapy alone, they supported adjuvant treatment for all patients, consistent with registry data suggesting improved outcomes with any adjuvant therapy[28].

The large cohort enabled exploration of disease heterogeneity within a single trial. Although this trial was negative for the primary endpoint of OS, it prospectively validated prognostic molecular biomarkers previously identified only retrospectively in single-center studies in a homogeneously treated population: H3.1-K27M as a favorable biomarker for survival and *TP53* mutations as a strong adverse prognostic biomarker[22,28,50]. *TP53* mutations define a higher-risk, radioresistant and more aggressive subgroup that should be considered for stratification in future trial designs.

No significant survival differences were observed among treatment arms, although median OS was slightly longer with everolimus compared to dasatinib, with median OS of 11.3 months (95% CI: 10.3–13.4) versus 9.4 months (95% CI: 8.2–10.8), respectively. OS with everolimus plus radiotherapy compared favorably to radiotherapy-only trials[51] and was slightly above the published registry data when taking the same starting point—that is, at radiological diagnosis[28]. Notably, four very-long-term survivors were observed, all treated with mTOR inhibitors. Everolimus was associated with fewer skin, ocular and infectious toxicities and fewer treatment discontinuations. Patients harboring PIK3/AKT/MTOR pathway mutations, an mTOR activation gene expression signature or 1q gain derived greater benefit from everolimus than from dasatinib, with median OS of 14 months versus 9 months, respectively. These findings identify a clinically important theranostic biomarker for future trials, consistent with breast cancer trials[52]. The role of the PI3K/AKT/MTOR pathway in DIPG was described in previous studies, including CRISPR–Cas9 loss-of-function screen, preclinical studies[32,53–55], and combination strategies may be clinically feasible given the favorable toxicity profile of everolimus. Collectively, these data support the selection of everolimus as the standard arm for a next iteration of the BIOMEDE adaptive trial. The adaptative design enabled identification of this winner arm for comparison with emerging agents, and promising

Fig. 5 | Response to therapy according to PI3K/AKT/MTOR alterations. **a**, Forest plot comparing the differential effects of everolimus and dasatinib on OS according to the presence or absence of relevant biomarkers among the 147 patients with biological evaluation allocated to the everolimus versus dasatinib comparison ($n = 67$ versus $n = 80$, respectively). Chrom_1q_2gain indicates concomitant gains of chromosome 1q and 2 together. HPI3K refers to the level of expression of the PI3K/AKT/MTOR pathway. AKTmTOR denotes the presence or absence of mutations in the PI3K/AKT/MTOR pathway. Interaction *P* values were considered significant when lower than 0.1. The diamond represents the overall treatment effect and its width the 95% CI. Each horizontal line represents the hazard ratio (square) and its 95% CI of treatment effect for each modality of a covariate. An arrow indicates that the upper limit of the 95% CI is outside the margins. The vertical line represents the null hypothesis of no treatment effect (hazard ratio = 1). NS, no significant modulation of the level of expression of genes belonging to PI3K/AKT/MTOR. **b**, Forest plot comparing the differential effects of everolimus and dasatinib on PFS according to the presence or absence of relevant biomarkers. To confirm the impact of theranostic biomarkers on the response to everolimus, we compiled an independent cohort of 31 patients with DIPG with available sequencing data who were treated at Gustave Roussy with sirolimus or everolimus either before trial initiation or after randomization was stopped. The diamond represents the overall treatment effect and its width the 95% CI. Each horizontal line represents the hazard ratio (square) and its 95% CI of treatment effect for each modality of a covariate. An arrow indicates that the upper limit of the 95% CI is outside the margins. The vertical line represents the null hypothesis of no treatment effect (hazard ratio = 1). **c**, OS in patients without PI3K/AKT/MTOR alterations, stratified by randomized treatment. **d**, OS in patients with PI3K/AKT/MTOR alterations, stratified by randomized treatment (two-sided interaction test). **e**, PFS in patients without PI3K/AKT/MTOR alterations, stratified by randomized treatment. **f**, PFS in patients with PI3K/AKT/MTOR alterations, stratified by randomized treatment (two-sided interaction test). **g**, Oncoplot showing SNV alterations in genes involved in PI3K/AKT/MTOR pathway in DMG, ranked from left to right according to decreasing GSVA pathway scores. SNV alterations from patients without available RNA-seq data are shown on the right. Evts, events; HR, hazard ratio; Pts, patients.

https://doi.org/10.1038/s41591-026-04354-1

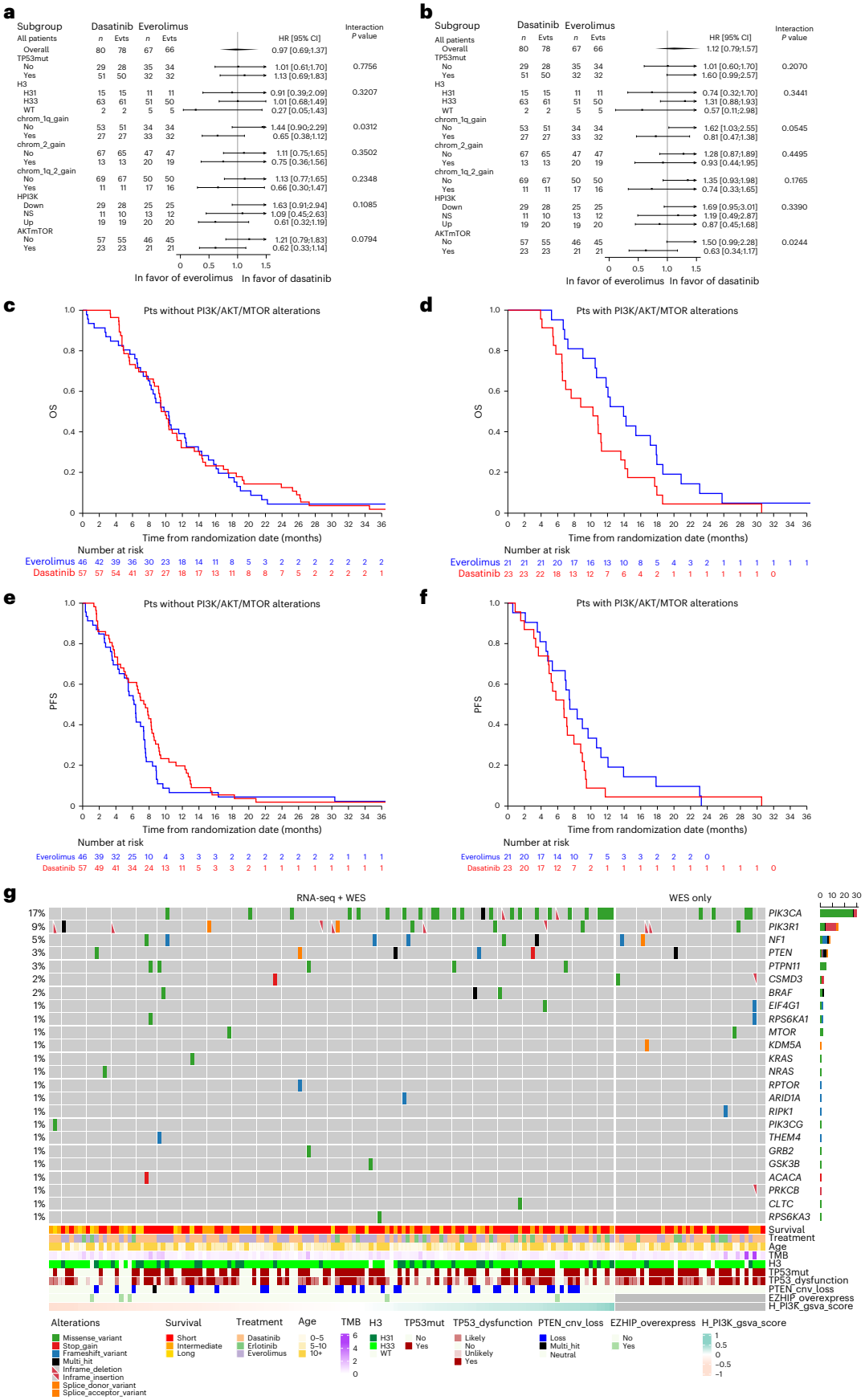

preliminary results with ONC201 led to the initiation of a randomized phase 3 trial comparing everolimus to ONC201.

Therapies have recently emerged, including chimeric antigen receptor (CAR) T cells targeting B7-H3 or GD2 and ONC201 (ref. 56). Combining everolimus with CAR T cells may enhance T cell responses by limiting exhaustion driven by mTOR-dependent metabolic activation[57]. Although preclinical studies suggest combining mTOR inhibition with ONC201 (refs. 32,55), ONC201 induces cytochrome P450 3A4 and may increase the clearance of CYP3A4 substrates such as everolimus in humans.

Comprehensive molecular profiling enabled refined identification of outcome-associated tumor subtypes. Tumors with the poorest prognosis harbored *TP53* mutations and were less likely to show common numerical chromosomal gains (1q and whole chromosome 2), instead exhibiting numerous structural alterations. This is consistent with a previous report linking complex structural variant signatures in high-grade gliomas to shorter survival[58]. Gene expression analyses revealed a more immunosuppressive phenotype in these tumors. Although dominant-negative *TP53* mutations with LOH were the most frequent cause of p53 dysfunction, other recurrent alterations likely contributed, including mutually exclusive truncating *PPM1D* mutations[37,59] (11%) or *TP53BP1* loss (14.5%), which may contribute to genome instability[60].

Patients surviving more than 2 years were more likely to harbor tumors with an activated immune microenvironment, characterized by enrichment of Mg-TAM secreting TNFSF12/TWEAK and lower expression of immunosuppressive cytokines (TGFβ and KLF12), compared to short-term survivors whose tumors more frequently harbored *TP53* mutations and overexpressed natural killer cell inhibitory markers such as KLRC1 and TGFβ. The TME of DIPG and DMG has been largely described as immunosuppressive, including reduced TNF signaling, suggesting that myeloid infiltration—typically composed of unpolarized TAMs with limited cytokine secretion—may be predominantly protumoral[48,61–63]. A recent study from the Toronto group reported substantial intertumoral TME heterogeneity, with 9% of DMGs displaying higher inflammation scores[64], although no correlation with survival was observed. This discrepancy may reflect the inclusion of patients with both supratentorial DMGs and DIPGs with likely distinct microenvironments[65]. Consistently, that later study also reported lower inflammatory scores in DMGs with missense *TP53* mutations, in line with our observation of a more immunosuppressive TME in *TP53*-mutant tumors. Collectively, these findings suggest that shifting TME toward a proinflammatory state could confer a survival advantage[48].

Long-term survivors exhibited a metabolic shift toward oxidative phosphorylation compared to short-term survivors, supporting a reversed Warburg effect that may limit tumor growth. The relevance of this metabolic switch is further highlighted by an unexpected mutational combination observed in some long-term survivors. Specifically, the presence of an *IDH1* R132C mutation was associated with prolonged survival in two patients, suggesting potential interference between IDH1-driven and H3K27M-driven oncogenic pathways in DIPG. The oncometabolite D-2HG produced by mutant *IDH1* increases H3K27me3 by inhibiting H3K27 demethylases and is toxic to H3.3K27M cells[66]. Thus, H3K27M and IDH mutations hijack conserved metabolic pathways in opposing ways to sustain their epigenetic state. The coexistence of these alterations in several patients challenges the proposed mutual exclusivity and synthetic lethality of H3K27M and IDH mutations[66]. Although oncogenic interference has also been reported for MAPK-activating *FGFR1* and *BRAF* V600E mutations in DMG, particularly outside the brainstem and associated with better survival[67], such combinations were not encountered in this cohort.

Finally, we show that up to 10% of patients with radiologically diagnosed DIPG represent alternative entities, supporting trials only in biologically confirmed diffuse brainstem gliomas[68].

One limitation of the study is that it was designed more than 10 years ago, when knowledge of DIPG biology was still scarce. Nevertheless, the PIK3/AKT/MTOR pathway remains one of the major therapeutic targets in this disease, as shown in our study. Another limitation is the use of first-generation inhibitors, which have been since improved in some instances. However, this trial was able to demonstrate a survival advantage in a selected population—namely, patients with MTOR alterations or activation treated with everolimus.

In conclusion, this large randomized study identified a subgroup of patients with a very-poor-prognosis DIPG linked to *TP53* alterations and defined predictors for sensitivity to everolimus, informing future trials using PI3K/AKT/MTOR pathway inhibitors. Notably, we report, in this prospective trial, long-term survivors with biologically proven DIPG. We also identified specific gene expression signature and immune-proficient myeloid microenvironment in patients surviving more than 2 years, supporting further development of immunotherapies targeting these immune effectors.

Online content

Any methods, additional references, Nature Portfolio reporting summaries, source data, extended data, supplementary information, acknowledgements, peer review information; details of author contributions and competing interests; and statements of data and code availability are available at https://doi.org/10.1038/s41591-026-04354-1.

References

1. Bender, S. et al. Reduced H3K27me3 and DNA hypomethylation are major drivers of gene expression in K27M mutant pediatric high-grade gliomas. *Cancer Cell* **24**, 660–672 (2013).
2. Castel, D. et al. Transcriptomic and epigenetic profiling of 'diffuse midline gliomas, H3 K27M-mutant' discriminate two subgroups based on the type of histone H3 mutated and not supratentorial or infratentorial location. *Acta Neuropathol. Commun.* **6**, 117 (2018).
3. Jain, S. U. et al. PFA ependymoma-associated protein EZHIP inhibits PRC2 activity through a H3 K27M-like mechanism. *Nat. Commun.* **10**, 2146 (2019).
4. Mariet, C. et al. Posterior fossa ependymoma H3 K27-mutant: an integrated radiological and histomolecular tumor analysis. *Acta Neuropathol. Commun.* **10**, 137 (2022).
5. Wu, G. et al. Somatic histone H3 alterations in pediatric diffuse intrinsic pontine gliomas and non-brainstem glioblastomas. *Nat. Genet.* **44**, 251–253 (2012).
6. Lewis, P. W. et al. Inhibition of PRC2 activity by a gain-of-function H3 mutation found in pediatric glioblastoma. *Science* **340**, 857–861 (2013).
7. Castel, D. et al. Histone H3 wild-type DIPG/DMG overexpressing *EZHIP* extend the spectrum diffuse midline gliomas with PRC2 inhibition beyond H3-K27M mutation. *Acta Neuropathol.* **139**, 1109–1113 (2020).
8. Coutel, Y. [Infiltrating glioblastoma of the brain stem in an 8-year-old child; normalization of the pneumoencephalogram after radiotherapy]. *Rev. Otoneuroophtalmol.* **31**, 119–123 (1959).
9. Roujeau, T. et al. Stereotactic biopsy of diffuse pontine lesions in children. *J. Neurosurg.* **107**, 1–4 (2007).
10. Caretti, V. et al. Human pontine glioma cells can induce murine tumors. *Acta Neuropathol.* **127**, 897–909 (2014).
11. Salloum, R. et al. Characterizing temporal genomic heterogeneity in pediatric high-grade gliomas. *Acta Neuropathol. Commun.* **5**, 78 (2017).
12. Nikbakht, H. et al. Spatial and temporal homogeneity of driver mutations in diffuse intrinsic pontine glioma. *Nat. Commun.* **7**, 11185 (2016).

13. Zarghooni, M. et al. Whole-genome profiling of pediatric diffuse intrinsic pontine gliomas highlights platelet-derived growth factor receptor α and poly (ADP-ribose) polymerase as potential therapeutic targets. *J. Clin. Oncol.* **28**, 1337–1344 (2010).
14. Puget, S. et al. Mesenchymal transition and PDGFRA amplification/mutation are key distinct oncogenic events in pediatric diffuse intrinsic pontine gliomas. *PLoS ONE* **7**, e30313 (2012).
15. Truffaux, N. et al. Preclinical evaluation of dasatinib alone and in combination with cabozantinib for the treatment of diffuse intrinsic pontine glioma. *Neuro Oncol.* **17**, 953–964 (2015).
16. Geoerger, B. et al. Innovative Therapies for Children with Cancer pediatric phase I study of erlotinib in brainstem glioma and relapsing/refractory brain tumors. *Neuro Oncol.* **13**, 109–118 (2011).
17. Gilbertson, R. J. et al. ERBB1 is amplified and overexpressed in high-grade diffusely infiltrative pediatric brain stem glioma. *Clin. Cancer Res.* **9**, 3620–3624 (2003).
18. Grasso, C. S. et al. Functionally defined therapeutic targets in diffuse intrinsic pontine glioma. *Nat. Med.* **21**, 555–559 (2015).
19. Geoerger, B. et al. Phase II trial of temsirolimus in children with high-grade glioma, neuroblastoma and rhabdomyosarcoma. *Eur. J. Cancer* **48**, 253–262 (2012).
20. Pollack, I. F. et al. A phase II study of gefitinib and irradiation in children with newly diagnosed brainstem gliomas: a report from the Pediatric Brain Tumor Consortium. *Neuro Oncol.* **13**, 290–297 (2011).
21. Broniscer, A. et al. Phase I trial, pharmacokinetics, and pharmacodynamics of vandetanib and dasatinib in children with newly diagnosed diffuse intrinsic pontine glioma. *Clin. Cancer Res.* **19**, 3050–3058 (2013).
22. Castel, D. et al. Histone *H3F3A* and *HIST1H3B* K27M mutations define two subgroups of diffuse intrinsic pontine gliomas with different prognosis and phenotypes. *Acta Neuropathol.* **130**, 815–827 (2015).
23. Chassot, A. et al. Radiotherapy with concurrent and adjuvant temozolomide in children with newly diagnosed diffuse intrinsic pontine glioma. *J. Neurooncol.* **106**, 399–407 (2012).
24. Lobon-Iglesias, M. J. et al. Diffuse intrinsic pontine gliomas (DIPG) at recurrence: is there a window to test new therapies in some patients? *J. Neurooncol.* **137**, 111–118 (2018).
25. Rubovszky, G. The role of everolimus in metastatic breast cancer and possibilities of moving forward—a narrative review. *Ann. Transl. Med.* **12**, 68 (2024).
26. Haas-Kogan, D. A. et al. Everolimus for children with recurrent or progressive low-grade glioma: results from the phase II PNOC001 trial. *J. Clin. Oncol.* **42**, 441–451 (2024).
27. Bailey, S. et al. Diffuse intrinsic pontine glioma treated with prolonged temozolomide and radiotherapy—results of a United Kingdom phase II trial (CNS 2007 04). *Eur. J. Cancer* **49**, 3856–3862 (2013).
28. Hoffman, L. M. et al. Clinical, radiologic, pathologic, and molecular characteristics of long-term survivors of diffuse intrinsic pontine glioma (DIPG): a collaborative report from the International and European Society for Pediatric Oncology DIPG Registries. *J. Clin. Oncol.* **36**, 1963–1972 (2018).
29. Mackay, A. et al. Integrated molecular meta-analysis of 1,000 pediatric high-grade and diffuse intrinsic pontine glioma. *Cancer Cell* **32**, 520–537 (2017).
30. Mueller, S. et al. A pilot precision medicine trial for children with diffuse intrinsic pontine glioma—PNOC003: a report from the Pacific Pediatric Neuro-Oncology Consortium. *Int. J. Cancer* **145**, 1889–1901 (2019).
31. Mateos, M. K. et al. Germline analysis of an international cohort of pediatric diffuse midline glioma patients. *Neuro Oncol.* **27**, 1849–1863 (2025).
32. Duchatel, R. J. et al. PI3K/mTOR is a therapeutically targetable genetic dependency in diffuse intrinsic pontine glioma. *J. Clin. Invest.* **134**, e170329 (2024).
33. Thatikonda, V. et al. Comprehensive analysis of mutational signatures reveals distinct patterns and molecular processes across 27 pediatric cancers. *Nat. Cancer* **4**, 276–289 (2023).
34. Gröbner, S. N. et al. The landscape of genomic alterations across childhood cancers. *Nature* **555**, 321–327 (2018).
35. Steele, C. D. et al. Signatures of copy number alterations in human cancer. *Nature* **606**, 984–991 (2022).
36. Boettcher, S. et al. A dominant-negative effect drives selection of *TP53* missense mutations in myeloid malignancies. *Science* **365**, 599–604 (2019).
37. Zhang, L. et al. Exome sequencing identifies somatic gain-of-function *PPM1D* mutations in brainstem gliomas. *Nat. Genet.* **46**, 726–730 (2014).
38. Wang, B., Matsuoka, S., Carpenter, P. B. & Elledge, S. J. 53BP1, a mediator of the DNA damage checkpoint. *Science* **298**, 1435–1438 (2002).
39. Shibata, A. & Jeggo, P. A. Roles for 53BP1 in the repair of radiation-induced DNA double strand breaks. *DNA Repair (Amst.)* **93**, 102915 (2020).
40. Mac Donald, A. et al. *KLRC1* knockout overcomes HLA-E-mediated inhibition and improves NK cell antitumor activity against solid tumors. *Front. Immunol.* **14**, 1231916 (2023).
41. Zhang, L., Gao, L., Shao, M. & Sun, G. Y. A MYC target long non-coding RNA GATA2-AS1 regulates non-small cell lung cancer growth. *Neoplasma* **66**, 954–962 (2019).
42. Wang, X. et al. Therapeutic targeting of FUBP3 phase separation by *GATA2-AS1* inhibits malate-aspartate shuttle and neuroblastoma progression via modulating SUZ12 activity. *Oncogene* **42**, 2673–2687 (2023).
43. Niu, Y. et al. LncRNA GATA2-AS1 suppresses esophageal squamous cell carcinoma progression via the mir-940/PTPN12 axis. *Exp. Cell Res.* **416**, 113130 (2022).
44. Snuderl, M. et al. Mosaic amplification of multiple receptor tyrosine kinase genes in glioblastoma. *Cancer Cell* **20**, 810–817 (2011).
45. Carvajal, L. A., Hamard, P.-J., Tonnessen, C. & Manfredi, J. J. E2F7, a novel target, is up-regulated by p53 and mediates DNA damage-dependent transcriptional repression. *Genes Dev.* **26**, 1533–1545 (2012).
46. Yang, R. et al. E2F7–EZH2 axis regulates PTEN/AKT/mTOR signalling and glioblastoma progression. *Br. J. Cancer* **123**, 1445–1455 (2020).
47. Motevasseli, M. et al. Distinct tumor–TAM interactions in IDH-stratified glioma microenvironments unveiled by single-cell and spatial transcriptomics. *Acta Neuropathol. Commun.* **12**, 133 (2024).
48. Andrade, A. F. et al. Immune landscape of oncohistone-mutant gliomas reveals diverse myeloid populations and tumor-promoting function. *Nat. Commun.* **15**, 7769 (2024).
49. Feng, A. et al. Homeobox A7 promotes esophageal squamous cell carcinoma progression through C-C motif chemokine ligand 2-mediated tumor-associated macrophage recruitment. *Cancer Sci.* **114**, 3270–3286 (2023).
50. Werbrouck, C. et al. TP53 pathway alterations drive radioresistance in diffuse intrinsic pontine gliomas (DIPG). *Clin. Cancer Res.* **25**, 6788–6800 (2019).
51. Park, J., Yea, J. W. & Park, J. W. Hypofractionated radiotherapy versus conventional radiotherapy for diffuse intrinsic pontine glioma: a systematic review and meta-analysis. *Medicine (Baltimore)* **99**, e22721 (2020).
52. André, F. et al. Molecular alterations and everolimus efficacy in human epidermal growth factor receptor 2-overexpressing metastatic breast cancers: combined exploratory biomarker analysis from BOLERO-1 and BOLERO-3. *J. Clin. Oncol.* **34**, 2115–2124 (2016).

53. Miyahara, H. et al. The dual mTOR kinase inhibitor TAK228 inhibits tumorigenicity and enhances radiosensitization in diffuse intrinsic pontine glioma. *Cancer Lett.* **400**, 110–116 (2017).
54. Flannery, P. C. et al. Preclinical analysis of MTOR complex 1/2 inhibition in diffuse intrinsic pontine glioma. *Oncol. Rep.* **39**, 455–464 (2018).
55. Jackson, E. R. et al. ONC201 in combination with paxalisib for the treatment of H3K27-altered diffuse midline glioma. *Cancer Res.* **17**, OF1–OF17 (2023).
56. Venneti, S. et al. Clinical efficacy of ONC201 in H3K27M-mutant diffuse midline gliomas is driven by disruption of integrated metabolic and epigenetic pathways. *Cancer Discov.* **13**, 2370–2393 (2023).
57. Myers, D. R., Wheeler, B. & Roose, J. P. mTOR and other effector kinase signals that impact T cell function and activity. *Immunol. Rev.* **291**, 134–153 (2019).
58. Dubois, F. P. B. et al. Structural variants shape driver combinations and outcomes in pediatric high-grade glioma. *Nat. Cancer* **3**, 994–1011 (2022).
59. Khadka, P. et al. *PPM1D* mutations are oncogenic drivers of de novo diffuse midline glioma formation. *Nat. Commun.* **13**, 604 (2022).
60. Kilgas, S., Swift, M. L. & Chowdhury, D. 53BP1-the 'Pandora's box' of genome integrity. *DNA Repair (Amst.)* **144**, 103779 (2024).
61. Pachocki, C. J. & Hol, E. M. Current perspectives on diffuse midline glioma and a different role for the immune microenvironment compared to glioblastoma. *J. Neuroinflammation* **19**, 276 (2022).
62. Lieberman, N. A. P. et al. Characterization of the immune microenvironment of diffuse intrinsic pontine glioma: implications for development of immunotherapy. *Neuro Oncol.* **21**, 83–94 (2019).
63. Lin, G. L. et al. Non-inflammatory tumor microenvironment of diffuse intrinsic pontine glioma. *Acta Neuropathol. Commun.* **6**, 51 (2018).
64. Levine, A. B. et al. Immuno-oncologic profiling of pediatric brain tumors reveals major clinical significance of the tumor immune microenvironment. *Nat. Commun.* **15**, 5790 (2024).
65. Liu, I. et al. The landscape of tumor cell states and spatial organization in H3-K27M mutant diffuse midline glioma across age and location. *Nat. Genet.* **54**, 1881–1894 (2022).
66. Chung, C. et al. Integrated metabolic and epigenomic reprograming by H3K27M mutations in diffuse intrinsic pontine gliomas. *Cancer Cell* **38**, 334–349 (2020).
67. Auffret, L. et al. A new subtype of diffuse midline glioma, H3 K27 and BRAF/FGFR1 co-altered: a clinico-radiological and histomolecular characterisation. *Acta Neuropathol.* **147**, 2 (2023).
68. Pearson, A. D. et al. Paediatric strategy forum for medicinal product development in diffuse midline gliomas in children and adolescents ACCELERATE in collaboration with the European Medicines Agency with participation of the Food and Drug Administration. *Eur. J. Cancer* **217**, 115230 (2025).

Marie-Anne Debily[1,2,28] ✉, Gwenael Le Teuff[3,28], Thomas Kergrohen[1,28], Pascale Varlet[4], David Castel[1], Pierre Leblond[5], Darren Hargrave[6], Karsten Nysom[7], Klas Blomgren[8,9], Geoffrey Brian McCowage[10], Francisco Bautista[11,27], Dannis van Vuurden[12], Chris Jones[13], Alan Mackay[13], Elisa Izquierdo[13,14,15], David S. Ziegler[16], Angokai Moussa[3], Emilie Barret[1], Stephanie Puget[17], Kevin Beccaria[17], Kristian Aquilina[18], Laurent Riffaud[19], Stephanie Bolle[20], Samuel Abbou[1,21], Anne-Isabelle Bertozzi[22], Emilie De Carli[23], Nathalie Boddaert[24], Volodia Dangouloff-Ros[24], Raphael Calmon[24], Patricia Blanc[25], Gilles Vassal[1,21], Marie-Cécile Le Deley[26] & Jacques Grill[1,21] ✉

[1]INSERM 1360, Gustave Roussy, Université Paris-Saclay, Oncogenesis, Resistance and Therapeutic Targets of Pediatric Cancers, Team 'Genomics and Oncogenesis of Pediatric Brain Tumors', Villejuif, France. [2]Department of Biology, University Evry Paris-Saclay, Evry, France. [3]Department of Statistics and Epidemiology, Gustave Roussy, Villejuif, France. [4]Department of Neuropathology, Groupe Hospitalier Universitaire Paris-Psychiatrie et Neurosciences, Sainte-Anne Hospital, Paris, France. [5]Institut d'Hématologie et d'Oncologie Pédiatrique, Centre Léon Bérard, Lyon and Unité d'oncologie pédiatrique, Centre Oscar Lambret, Lille, France. [6]Great Ormond Street Institute of Child Health, University College London, London, UK. [7]Department of Pediatrics and Adolescent Medicine, Rigshospitalet Copenhagen University Hospital, Copenhagen, Denmark. [8]Department of Women's and Children's Health, Karolinska Institutet Stockholm, Stockholm, Sweden. [9]Pediatric Oncology, Karolinska University Hospital, Stockholm, Sweden. [10]Sydney Children's Hospitals Network, Westmead, New South Wales, Australia. [11]Department of Pediatric Hematology and Oncology, Hospital Infantil Universitario Nino Jesus, Madrid, Spain. [12]Princess Maxima Center for Pediatric Oncology, Utrecht, The Netherlands. [13]Division of Cancer Biology, The Institute of Cancer Research, London, UK. [14]Institute of Medical and Molecular Genetics (INGEMM), La Paz University Hospital, Madrid, Spain. [15]CIBERER-ISCIII, IdiPAZ-CNIO Translational Research Unit in Pediatric Hemato-Oncology, La Paz University Hospital Research Institute, Spanish National Cancer Center, Madrid, Spain. [16]Kids Cancer Centre, Sydney Children's Hospital, Randwick and School of Clinical Medicine, University of New South Wales and Children's Cancer Institute Australia, Lowy Cancer Research Centre, Sydney, New South Wales, Australia. [17]Pediatric Neurosurgery, Assistance Publique Hôpitaux de Paris, Hôpital Necker Enfants Malades, Université Paris Cité, Paris, France. [18]Department of Neurosurgery, Great Ormond Street Hospital, London, UK. [19]Department of Pediatric Neurosurgery, University Hospital, Rennes, France. [20]Centro de Protonterapia Quironsalud, Madrid, Spain. [21]Département de Cancérologie de l'Enfant et de l'Adolescent, Gustave Roussy, Université Paris-Saclay, Villejuif, France. [22]Pediatric Oncology Department, Children's Hospital, Toulouse University Hospital, Toulouse, France. [23]Department of Pediatric Oncology, University Hospital, Angers, France. [24]Pediatric Radiology

Department, Assistance Publique Hôpitaux de Paris, Hôpital Necker Enfants Malades and INSERM ERL UA10, INSERM U1163, Institut Imagine, Paris, France. [25]Charity Imagine for Margo, Paris, France. [26]Methodology and Biostatistics Unit, Centre Oscar Lambret, Lille, France. [27]Present address: Princess Maxima Center for Pediatric Oncology, Utrecht, The Netherlands. [28]These authors contributed equally: Marie-Anne Debily, Gwenael Le Teuff, Thomas Kergrohen. ✉e-mail: marie-anne.debily@gustaveroussy.fr; jacques.grill@gustaveroussy.fr

Methods

Patient cohort description

Human clinical samples and data were collected after written informed consent was obtained in accordance with the Declaration of Helsinki and approval from the relevant national and institutional review boards. Patients with brainstem tumors were enrolled in the BIOMEDE trial (NCT02233049) based on classical clinico-radiological characteristics: intrinsic brainstem tumors involving at least 50% of the pons and a short clinical history, defined as less than 3 months between first symptoms and diagnosis[69]. Initial informed consent was obtained to perform a stereotactic biopsy to ascertain the histological diagnosis and to conduct WES and RNA-seq of the tumor as well as WES of the matched blood samples. The diagnosis was confirmed by central pathology review led by P.V. When the diagnosis of a diffuse brainstem glioma with loss of H3K27me3, with or without an H3K27M mutation[22], was confirmed, a second informed consent was obtained for entry into the randomized phase 2 trial. Only patients with a confirmed histological diagnosis of DIPG were enrolled. Treatments were administered in combination with radiotherapy and in the adjuvant setting until disease progression or the occurrence of major toxicity. The list of centers that recruited patients in the study, as well as the number of patients per center, is provided in Supplementary Table 10.

Eligibility/non-eligibility criteria

Eligibility criteria for the BIOMEDE study (prescreening for the randomized subtrials).

- Diagnosis of DIPG (based on clinico-radiological criteria or histological confirmation if a biopsy was performed prior to study entry)
- Patients with NB-DMG, H3K27M-mutant, are eligible for the trial after biopsy or surgery. As biopsy or surgery is considered as standard practice for these tumor locations, specific informed consent for the biopsy is not required. Patient will provide informed consent after diagnosis to allow central pathology review and subsequent biomarker assessment.
- DIPG or NB-DMG at diagnosis: no prior chemotherapy for the present cancer and no prior cerebral radiotherapy
- Note: Metastatic disease is allowed. Patients with metastatic disease are eligible for the study (including the randomized trial) if a diagnosis of DIPG/NB-DMG is confirmed. In this case, radiotherapy must start within 3 weeks after biopsy, and targeted treatment will begin at the end of the radiotherapy.
- Age >6 months and <30 years. For children younger than 3 years, inclusion in the study and medical decisions should be discussed with the coordinating investigator.
- Eligible for biopsy or biopsy already performed for diagnostic purposes with tissue material available for biomarker assessment
- Eligible for cerebral radiotherapy
- Patient covered by health insurance, if required by national regulations
- Written informed consent provided by the patient and/or parents/legal representative for biomarker assessment and study registration

Non-eligibility criteria for the study.

- Spontaneous massive intratumor hemorrhage. Patients with postoperative bleeding may be eligible provided the hemorrhage is controlled. The same applies to other postoperative complications (for example, infection, cerebrospinal fluid leakage, incomplete wound closure and subdural collection).
- Any concomitant anticancer treatment not foreseen by this protocol
- Any other cancer within the past 5 years
- Uncontrolled intercurrent illness or active infection
- Any other comorbid condition that, in the investigator's opinion, would interfere with study participation
- Inability to comply with medical follow-up due to geographic, social or psychological reasons
- Failure to meet any of the eligibility criteria listed above
- Previous irradiation of the brainstem for another neoplasm
- Known congenital galactose intolerance, Lapp lactase deficiency or glucose-galactose malabsorption
- Lack of health insurance coverage accepted in the treating country, if required by national regulations
- Pregnant or breastfeeding women
- Note: Patients with known hypersensitivity to one of the study drugs or its excipients may still participate in the study and receive one of the other study drug(s).

Common eligibility criteria for the BIOMEDE randomized subtrials.

- Fulfilment of the study eligibility criteria (see above)
- Confirmed histological diagnosis of DIPG (WHO grade II, III and IV) or NB-DMG confirmed by central pathology review (including the assessment of H3K27me3 loss[70] by immunohistochemistry and/or the presence of a mutation in histone H3 variant genes). Patients lacking classical clinico-radiological diagnostic criteria but fulfilling the histological and biological criteria for DIPG are eligible for the trial. Pilocytic astrocytomas and gangliogliomas are not eligible. Patients with suspected DIPG without histological confirmation may be randomized if, and only if, imaging findings are typical of DIPG and the clinical history is short. Such cases must be centrally reviewed and approved. For NB-DMG cases, confirmation of the diagnosis of NB-DMG, H3K27M-mutant, by central pathology review is required prior to randomization.
- Life expectancy >12 weeks after initiation of study treatment
- Karnofsky performance status scale or Lansky Play Scale >50%. Performance status should not take neurological deficits per se into account. Note: Children and young adults with poorer performance status due to glioma-related motor paresis may be included.
- Absolute neutrophil count >1.5 × 10^9 per liter; platelets >100 × 10^9 per liter
- Total bilirubin <1.5× upper limit of normal (ULN); aspartate aminotransferase (AST) and alanine aminotransferase (ALT) <2.5× ULN
- Serum creatinine <1.5× ULN for age. If serum creatinine is >1.5× ULN, creatinine clearance must be >70 ml min^{-1} 1.73 m^{-2} (measured by EDTA radioisotope glomerular filtration rate or 24-hour urine collection).
- Normal coagulation tests within the local reference ranges
- No ongoing organ toxicity higher than grade 2 according to Common Terminology Criteria for Adverse Events version 4.0, particularly cardiovascular, pulmonary or renal disease (including, but not limited to, congenital long QT syndrome, nephrotic syndrome, glomerulopathy, uncontrolled high blood pressure despite adequate treatment, interstitial lung disease and pulmonary arterial hypertension). In cases of known or possible cardiac disease, a cardiological advice is required prior to inclusion in the randomized trial, as a preexisting cardiopathy represents a contraindication to dasatinib.
- Use of effective and appropriate contraception for patients (male and female) of reproductive potential throughout study participation and for 6 months after the end of treatment. Effective contraception is defined in Clinical Trial Facilitation Group guidelines 'Recommendations related to contraception and pregnancy testing in clinical trials' (Appendix 7).

- Negative pregnancy test (serum βHCG or urinary test) performed within the week prior to inclusion in sexually actives females of reproductive potential
- Written informed consent provided by the patient and/or parents/legal representative for treatment and randomization

Eligibility criteria for the subtrials. Eligibility criteria for the different subtrials were primarly based on biomarker assessment, as detailed below. In addition, contraindications to specific drugs were taken into account.

Study procedures (treatment allocation, statistical plan and sample size calculation)

The protocol was approved by the ethics commitee, Comité de protection des personnes d'Ile-de-France VII du Kremlin-Bicêtre (in June 2014), by the Agence nationale de sécurité des medicaments (EudraCT 2014-001929-32) and by the institutional review board of Gustave Roussy (CSET2014/2126).

Treatment allocation. The objective of the randomization process was to ensure that no child would be randomized to receive a drug for which the corresponding biomarker was negative in the tumor. Treatment allocation was based mainly on two biomarkers: EGFR expression (assessed in 95% of cases and overexpressed in 38.5%) and PTEN expression (assessed in 82.4% of cases, with PTEN loss observed in 96%), as no single biomarker could be identified for dasatinib (Fig. 1b). Indeed, many of the 60 known targets of dasatinib are expressed in DIPG[18]. For seven patients, the biomarkers were not fully informative, and these patients were randomized across the three treatment arms (R3). Patients randomized into the three subtrials are described in Extended Data Table 2. The populations used for the pairwise (two-by-two) drug comparisons subsequently were then constructed as shown in Fig. 1.

Randomization was performed centrally by the Gustave Roussy Biostatistics Unit, using online centralized randomization software (TENALEA version 2.2; Netherlands Cancer Institute), ensuring concealment of treatment allocation. For each subtrial, balanced randomization among treatment groups was carried out using a minimization algorithm and an online randomization software that accounted for biomarker status (EGFR overexpression versus EGFR unknown; PTEN loss versus PTEN unknown) and country, with a random parameter set at 0.8.

Statistical plan and sample size calculation. The treatment allocation rule was based on EGFR overexpression and loss of PTEN expression as determined by immunohistochemistry.

At the trial design stage, it was anticipated that:

- Biomarker results would be uninformative in 15% of cases
- Among tumors with informative material (85% of cases),
  - 90% would exhibit PTEN loss;
  - 50% would show EGFR overexpression;
  - The two biomarkers would be independent.

Consequently, the expected distribution of patients across the different subtrials was as follows:

- R1 trial, erlotinib versus dasatinib: 4.25%
- R2 trial, everolimus versus dasatinib: 38.25%
- R3 trial, erlotinib versus everolimus versus dasatinib: 38.25% + 15% = 63.25%
- Dasatinib cohort (not randomized): 4.25%

Because each patient in the R3 subtrial contributes to two of the three pairwise comparisons, the expected distribution of patients per randomized pairwise comparison was:

- 'Erlotinib versus Dasatinib' comparison: 100% of R1 + 2/3 of R3 = 40%
- 'Everolimus versus Dasatinib' comparison: 100% of R2 + 2/3 of R3 = 74%
- 'Erlotinib versus Everolimus' comparison: 2/3 of R3 = 36%

Consequently, the smallest pairwise comparison was the 'Erlotinib versus Everolimus' comparison, representing 36% of the randomized trial population, corresponding to approximately 90 patients if 250 patients were recruited into the randomized subtrials.

The expected distribution across the different subtrials and the three pairwise comparisons is shown in Fig. 1.

Survival analysis

The median follow-up was estimated with the reverse Kaplan–Meier method according to Schemper's method. OS (primary endpoint of the BIOMEDE trial), defined as the time from the date of randomization (for randomized group comparisons) to death from any cause, or to the date of last follow-up for alive patients, was estimated by the Kaplan–Meier method. For each of the three pairwise comparisons within the randomized trial, the relative treatment effect was estimated using the hazard ratio for death and its 95% CI, derived from a Cox proportional hazards model. The proportional hazards assumption underlying the hazard ratio estimate in Cox models was not formally tested because of the relatively small sample size and the observed survival curves (which crossed in the absence of clear treatment differences). The primary analysis was stratified by biomarker status (EGFR expression and PTEN loss). For the comparison of everolimus versus dasatinib, heterogeneity of treatment effects on OS and PFS was explored according to age group (<5 years, 5–10 years and ≥10 years), sex, EGFR overexpression (yes versusno versus unknown), PTEN loss (yes versus unknown) and histone status assessed by immunohistochemistry (wild-type versus H3.1-K27M versus H3.3-K27M). These subgroup effects were evaluated graphically using forest plots and formally tested using interaction tests. For the other comparisons, heterogeneity analyses could not be performed because of limited sample size. In the absence of a concurrent control group in the randomized trials, OS curves of each treatment group, irrespective of biomarker profile, were also compared with those of a historical control cohort. This historical control group comprised 66 patients with biopsy-proven DIPG treated who had received chemotherapy before initiation of the BIOMEDE trial, after exclusion of patients who had received any of the drugs included in the BIOMEDE protocol[23]. Comparisons between each treatment group and this synthetic control arm were performed using a one-sample log-rank test with a one-sided α level of 0.05 (ref. 71).

For prognostic factors analyses, OS from the date of randomization was compared using the log-rank test. Associations between prognostic classification schemes and OS were quantified using hazard ratios and 95% CIs estimated with Cox proportional hazards regression models. These models were adjusted for EGFR status (overexpression, negative and unknown), PTEN status (PTEN loss and unknown) and treatment group (dasatinib, erlotinib and everolimus), as these biomarkers were used for stratification in the BIOMEDE trial. Model goodness of fit and discriminant performance of the different prognostic classification schemes were assessed using (1) the Akaike information criterion (AIC) as the different prognostic classification schemes are not nested (lower AIC indicating better fit) and (2) Uno's concordance statistic (c-index; close to 1 indicating better discriminative ability), respectively. The standard error of Uno's c-index was estimated using 5,000 perturbation samples. The data cutoff date was 1 January 2019. All survival analyses were performed using SAS software version 9.4.

Protocol deviations

Data were monitored according to the monitoring plan. Protocol deviations were reported to the independent data monitoring committee to

ensure that these deviations had no impact on the safety of the patients or on the outcome of the study. Corrective measure are identified in the protocol amendment recapitulated in the last protocol version.

Response assessment

Clinical improvement was defined in the clinical report form by the treating physician's assessment based on the clinical signs present at diagnosis. A semiquantitative classification into three categories was applied: improved, stable or worsened. Radiological improvement was defined by the local radiologist's assessment based on Response Assessment in Neuro-Oncology (RANO) criteria. A semiquantitative classification into three categories was applied: improved, stable or worsened.

In cases of uncertainty regarding possible pseudoprogression, imaging was reviewed centrally prior to treatment decision-making. Pseudoprogression was considered when MRI changes occurred within the radiation field, typically presenting as new ring contrast enhancement, during the first 6 months after radiotherapy. The main characteristics supporting this diagnosis were increased perfusion early after radiotherapy[72,73] without increased infiltration outside the initial fields involved[72]. Confirmatory MRI demonstrating a decrease in enhancement on follow-up imaging was required. All doubtful cases were reviewed centrally in real time, blinded to treatment allocation. When true progression was identified on subsequent MRI, the date of progression was backdated to the date of the previous MRI.

Immunohistochemistry and fluorescence in situ hybridization analysis

All patients with an initial local diagnosis of DIPG were centrally reviewed according to the WHO 2007 classification by a BIOMEDE reference neuropathologist (P.V.) prior to enrollment. Four-micrometer sections were stained using an automated Discovery XT or Benchmark XT system (Ventana Medical Systems). The following primary antibodies were used: Ki67 (1:200, clone MIB-1, lot no. 41727891, cat. no. M7240; Dako), TP53 (1:5,000, clone DO-1, lot no. E3025, cat. no. SC6126X; CliniSciences), EGFR (1:200, clone EGFR 113, lot no. 6106573, cat. no. NCL-L-EGFR; Leica), PTEN (1:300, clone 6H2-1; Dako), H3K27M (1:5,000, clone EPR18340; Abcam), H3K27me3 (1:2,500, polyclonal, lot no. A0824D, cat. no. C15410195; Diagenode), phospho-S6 (1:400, polyclonal, lot no. 25, cat. no. 22115; Ozyme), phospho-AKT (1:100, polyclonal, lot no. 736E11, cat. no. 3787; Cell Signaling Technology), EZHIP (1:50, polyclonal, lot no. 61184, cat. no. HPA004003-3; Sigma-Aldrich), ATRX (1:100, clone BSB-108, lot no. 3298 TNF13, cat. no. B5B3297; Diagomics), GFAP (1:200, clone 6F2, lot no. 473002M, cat. no. MA1-35377; Dako) and OLIG2 (1:500, clone OLIG2, lot no. 000047004, cat. no. HPA 003254; Sigma-Aldrich). Accumulation of TP53, EGFR Hirsch score and loss of PTEN were assessed as previously described[74,75]. In brief, a Hirsch index equal to or above 150 was considered indicative of positive overexpression, and PTEN loss in tumor cells was considered only if the internal control (vessels) was positive. External positive and negative controls were included for all antibodies.

Fluorescence in situ hybridization (FISH) analysis was performed on interphase nuclei following standard procedures and the manufacturer's instructions. *PDGFRA* gene copy number was assessed using the centromeric and locus-specific probe PDGFRA/CEN4p (Abnova).

Signals were scored in at least 100 non-overlapping, intact interphase nuclei per case. Gene copy number per nucleus was recorded as follows: one copy, two copies, copy number gain (three copies) and amplification (four or more copies or innumerable clusters). Copy gain or amplification was considered significant if detected in more than 10% of nuclei. Results were recorded using a DM600 fluorescence microscope (Leica Biosystems) equipped with appropriate filters, a CCD camera and digital imaging software from Leica (CytoVision, version 7.4).

Tumor DNA preparation

Tumor DNA was extracted from frozen material using AllPrep DNA/RNA, and blood DNA was extracted using PAXgene Blood DNA kits, according to the manufacturer's instructions (Qiagen). Purified DNA was quantified using the Qubit Broad Range double-stranded DNA assay (Life Technologies).

WES

Library preparation, exome capture and sequencing were performed by IntegraGen SA. In brief, libraries were prepared from 150 ng of fragmented genomic DNA using the NEBNext Ultra DNA Library Prep Kit for Illumina (New England Biolabs). Exome sequences were captured using the SureSelect Human Clinical Research Exome V1 & V2 kits (Agilent Technologies) followed by paired-end 75-bp massively parallel sequencing on an Illumina NextSeq 500, achieving a mean coverage of 60× in the blood and 110× in tumor samples. For English patients, sequencing was performed at the Genomics Facility of the Institute of Cancer Research on a NextSeq 500 using SureSelect Human Exome V5 (Agilent Technologies) with a mean coverage of 78× in the blood and 239× in the tumor samples.

After base calling using Real-Time Analysis (RTA2) software, sequence quality was assessed with FastQC (version 11.0.3) and FastQ Screen. Reads were mapped to the human genome build (GRCh37) using the BWA-MEM tool. Filtering and recalibration were conducted with Picard tools following GATK version 3.6 best practices. FASTQ files were also analyzed with the pipeline nf-core/sarek version 3.4.0 (https://doi.org/10.1093/nargab/lqae031), and reads were mapped to human genome build GRCh38 using the BWA-MEM tool, followed by GATK4 best practice markduplicate and recalibration. Raw data were deposited in the European Genome-phenome Archive (EGAS50000001164).

Somatic variant calling and mutational signature

Somatic mutations, including SBSs and indels, were detected by Mutect2. Variants were annotated by Variant Effected Predictor (version 105)[76] using dbSNP version 153 and subsequently converted to MAF files for analysis by Maftools[77]. Somatic variations were selected if they passed all quality control filters, had a sequencing depth in both normal and tumor samples above 10, had a VAF >5% with a minimum of five supporting reads in tumor and had a VAF <3% with a maximum of three supporting reads in the matching normal samples. Intronic, untranslated regions (UTRs) and synonymous variations were excluded as well as SNVs with a frequency higher than 1% in healthy donors according to the 1000 Genomes Project (1000G_phase3) and gNOMAD 2.1.

Mutational signature analysis was performed with the Sigminer package (version 2.3.1) following standard pipeline. Mutational similarity with COSMIC version 3 (ref. 78) was estimated using the sig.fit function in the Sigminer package, and signatures likely representing sequencing artifact were filtered out. Somatic interaction analyses, including mutual exclusivity or co-occurrence, were performed using pairwise Fisher's exact tests.

SNV germline analysis

Germline variant calling was performed with Strelka and annotated with VEP (version 114.0) and annotation: 1000 Genomes, GRCh38.p14, ClinVar 202409, COSMIC 100, dbSNP 156, GENCODE 48, gnomADe version 4.1, gnomADg version 4.1, PolyPhen 2.2.3 and SIFT 6.2.1. Raw germline variants were initially filtered to remove variants with a VAF below 40% and synonymous changes. Recurrent germline variants were selected if their population frequency was below 1/1,000 in gNOMAD, predicted pathogenic by at least four independent tools and observed in at least three distinct patients.

Copy number analysis

CNVs were investigated using CNVkit in the nf-core/sarek pipeline. Clustering and visualization were performed with R packages tidyverse

and ComplexHeatmap. Gains and losses were defined as $\log_2$ ratio above 0.2 or below −0.2, respectively.

Samples with log2 ratio above 0.20 for at least 60% of the 1q chromosome arm or the entire chromosome 2 were labeled as 'chrs 1q gain' and 'chrs2 gain', respectively, for subsequent analyses. Genomic amplification was defined as regions associated with a $\log_2$ ratio >1.5.

Copy number signatures are defined using a 48-category context classification scheme, incorporating LOH status, total copy number state and segment length. Signatures were compared to the 25 reference COSMIC v3.2 CN signatures with R package Sigminer v2.3.1 (function sig.fit with sig_db=CN_TCGA).

Chromothripsis scores (CSs) were computed as previously described[79], based on the presence of tens to hundreds of locally clustered segmental losses interspersed with regions of stable copy number: $CS = \sum_{Chr} N^2 OsCN$, where N is square number of patterns '2–1–2' CNA.

The chromothripsis state score was as previously published[80].

The chromothripsis state score was computed according to Korbel and Campbell[79], with $\sum ChrN^2OsCN$

where N^2OsCN is the number of oscillating copy number pattern '2–1–2' for each chromosome.

Transcriptomic analysis

Poly(A)-containing mRNA molecules were purified from 100 ng of total RNA using poly(T) oligo-attached magnetic beads (NEBNext Poly(A) mRNA Magnetic Isolation Kit; New England Biolabs). Libraries were prepared using the NEBNext Ultra II Directional RNA Library Prep Kit (New England Biolabs) and sequenced on an Illumina NovaSeq to generate 100-bp paired-end reads.

Raw data were processed using the nf-core/RNAseq pipeline (version 3.10), with STAR for mapping step and Salmon for quantification against the GRCh38 genome with GENCODE version 32 annotation.

Pathway activity was assessed using the R GSVA package (version 1.50.00) with log-transformed transcripts per million (TPM) gene expression values. Deconvolution of bulk RNA-seq was performed using CIBERSORTx with default parameters. Human brain atlas and immune landscape data[81] were integrated using Harmony, and the 10,000 most variable genes were selected for signature definition.

Statistical analysis methodology for the biomarker studies

Biomarker studies were prespecified in the protocol as exploratory endpoints. These included previously reported prognostic biomarkers (for example, age, TP53 mutation and histone H3 mutation type: H3.3 versus H3.1 versus WT/EZHIP positive) and the identification of biomarkers associated with survival. Biomarkers associated with response to specific treatment arm were also evaluated.

All analyses were performed in R (version 4.3.3) using the ggpubr package.

Continuous variables (absolute values and changes from baseline) were summarized with box plots: center line, median; box limits, upper and lower quartiles; whiskers, 1.5× IQR; and points, outliers.

Changes from baseline for continuous variables (for example, COSMIC signatures and cell proportions in bulk RNA-seq deconvolution) were analyzed using paired two-sample *t*-tests. Differences between clinical and pathological categories were assessed using Fisher's exact test, and differences in the number of genomic segments detected by CNA analysis were evaluated by Wilcoxon test.

To describe the genomic profile, patients were categorized a priori into three age groups: younger than 5 years, strictly between 5 years and 10 years and older than 10 years. For survival analyses, patients were categorized post hoc into three groups: OS less than 1 year, OS between 1 year and 2 years and OS more than 2 years. Comparisons between the extreme survival groups were performed to identify gene alterations and gene expression signatures associated with survival.

Specific statistical procedures for each analysis are detailed in the figure legends. Sex was included in all clinical multivariate analyses. Specifically, we assessed whether sex was associated with theranostic biomarkers. As no significant association was identified, these results were not included in this paper. However, sex information will be provided when individual-level data are shared. We did not disaggregate the biological data by sex, as doing so would have substantially reduced the statistical power of the analyses. Moreover, to our knowledge, there is currently no evidence in the literature suggesting that sex influences tumor biology or patient outcomes in this context.

Reporting summary

Further information on research design is available in the Nature Portfolio Reporting Summary linked to this article.

Data availability

The analyses reported in this paper are based on a data cutoff of 2022, except for long-term survivor data, which were updated in September 2025. Genomic data are available through the European Genome-phenome Archive (EGAS50000001164). The list of variables in the trial database can be obtained upon reasonable request. Clinical data (sex, age, OS and PFS) will be available upon reasonable request through the signature of a data transfer agreement because these data are sensitive and belong to the sponsor of the study. Radiologic data, including diagnosis and follow-up imaging, are currently being uploaded and stored to an imaging repository at the Centre pour l'Acquisition et le Traitement des Images (CATI) (Neurospin data center in the CEA Paris-Saclay). The clinical and radiological data will be accessible upon reasonable request from the corresponding authors provided that the proposed study is not in competition with the current project of the consortium. A short turnover of 2 weeks to obtain the answer to the request is anticipated. Source data are provided with this paper.

References

69. Cohen, K. J., Jabado, N. & Grill, J. Diffuse intrinsic pontine gliomas-current management and new biologic insights. Is there a glimmer of hope? *Neuro Oncol.* **19**, 1025–1034 (2017).
70. Louis, D. N. et al. The 2021 WHO Classification of Tumors of the Central Nervous System: a summary. *Neuro Oncol.* **23**, 1231–1251 (2021).
71. Wu, J. Single-arm phase II cancer survival trial designs. *J. Biopharm. Stat.* **26**, 644–656 (2016).
72. Calmon, R. et al. Cerebral blood flow changes after radiation therapy identifies pseudoprogression in diffuse intrinsic pontine gliomas. *Neuro Oncol.* **20**, 994–1002 (2018).
73. Calmon, R. et al. Multimodal magnetic resonance imaging of treatment-induced changes to diffuse infiltrating pontine gliomas in children and correlation to patient progression-free survival. *Int. J. Radiat. Oncol. Biol. Phys.* **99**, 476–485 (2017).
74. Idoate, M. A., Echeveste, J., Diez-Valle, R., Lozano, M. D. & Aristu, J. Biological and clinical significance of the intratumour heterogeneity of PTEN protein expression and the corresponding molecular abnormalities of the *PTEN* gene in glioblastomas. *Neuropathol. Appl. Neurobiol.* **40**, 736–746 (2014).
75. Varlet, P. et al. WHO grade has no prognostic value in the pediatric high-grade glioma included in the HERBY trial. *Neuro Oncol.* **22**, 116–127 (2020).
76. McLaren, W. et al. The Ensembl Variant Effect Predictor. *Genome Biol.* **17**, 122 (2016).
77. Mayakonda, A., Lin, D.-C., Assenov, Y., Plass, C. & Koeffler, H. P. Maftools: efficient and comprehensive analysis of somatic variants in cancer. *Genome Res.* **28**, 1747–1756 (2018).
78. Alexandrov, L. B., Nik-Zainal, S., Wedge, D. C., Campbell, P. J. & Stratton, M. R. Deciphering signatures of mutational processes operative in human cancer. *Cell Rep.* **3**, 246–259 (2013).

79. Korbel, J. O. & Campbell, P. J. Criteria for inference of chromothripsis in cancer genomes. *Cell* **152**, 1226–1236 (2013).
80. Wang, S. et al. Copy number signature analysis tool and its application in prostate cancer reveals distinct mutational processes and clinical outcomes. *PLoS Genet.* **17**, e1009557 (2021).
81. Pombo Antunes, A. R. et al. Single-cell profiling of myeloid cells in glioblastoma across species and disease stage reveals macrophage competition and specialization. *Nat. Neurosci.* **24**, 595–610 (2021).

Acknowledgements

The authors would like to thank the children enrolled in the trial and their families as well as the investigators who treated the patients in the BIOMEDE trial from participating countries (France, United Kingdom, Australia, Spain, Denmark, Sweden and The Netherlands). For the clinical study, we also acknowledge the support of the Institut National du Cancer (Programme Hospitalier de Recherche Clinique, grant 11-114); Imagine for Margo; the Gustave Roussy Foundation (support of the Lemos family) (to J.G.); the Danish Childhood Cancer Foundation (grant no. 2015-13), for the conduct of the trial in Denmark; INTHEOS, for the conduct of the trial in Spain; Novartis, Bristol Myers Squibb and Roche, for drug supply; and Novartis France, for grant support. For the ancillary studies, J.G. acknowledges funding from Imagine for Margo, Etoile de Martin, Ligue Contre Le Cancer Val de Marne and Haute Savoie committees, and C.J. acknowledges funding from Abbie's Army, the CRIS Cancer Foundation and Cancer Research UK (DRCRPG-Nov21\100002 and C13468/A23536). None of the funders had any role in the analysis of the data.

Author contributions

Conception or design of the work: M.-A.D., D.H., K.N., S.P., K.A., S.B., N.B., P.B., G.V., M.-C.L.D. and J.G. Acquisition of data: M.-A.D., P.V., D.C., P.L., D.H., K.N., K. Blomgren, G.B.M., F.B., D.v.V., C.J., D.S.Z., K. Beccaria, L.R., S.B., S.A., A.-I.B., E.D.C. and V.D.-R. Analysis: M.-A.D., G.L.T., T.K., C.J., A. Mackay, E.I., A. Moussa, E.B., V.D.-R. and R.C. Interpretation of data: M.-A.D., G.L.T., G.V., P.V., V.D.-R., M.-C.L.D. and J.G. Drafting of the work: M.-A.D., G.L.T., M.-C.L.D. and J.G. Substantial revision of the manuscript: G.L.T., P.V., D.C., P.L., D.H., K.N., K. Blomgren, G.B.M., F.B., D.v.V., C.J., S.B., P.B.B. and G.V. All authors approved the submitted version. All authors have agreed to be personally accountable for their own contributions and to ensure that any questions related to the accuracy or integrity of any part of the work, even parts in which they were not personally involved, are appropriately investigated and resolved and that the resolution is documented in the literature.

Competing interests

The authors declare that three drugs (everolimus, erlotinib and dasatinib) were supplied free of charge by the pharmaceutical companies (Novartis, F. Hoffman-La Roche and Bristol Myers Squibb, respectively). Novartis also provided a grant to support the conduct of the study. None of these companies had any influence on the authors' judgments or actions with regard to the objective presentation, analysis and interpretation of the data. The authors declare no other competing interests related to this study.

Additional information

Extended data is available for this paper at https://doi.org/10.1038/s41591-026-04354-1.

Supplementary information The online version contains supplementary material available at https://doi.org/10.1038/s41591-026-04354-1.

Correspondence and requests for materials should be addressed to Marie-Anne Debily or Jacques Grill.

Peer review information *Nature Medicine* thanks Jasia Mahdi, Adam Green and the other, anonymous, reviewer(s) for their contribution to the peer review of this work. Primary Handling Editor: Saheli Sadanand, in collaboration with the *Nature Medicine* team. Peer reviewer reports are available.

https://doi.org/10.1038/s41591-026-04354-1

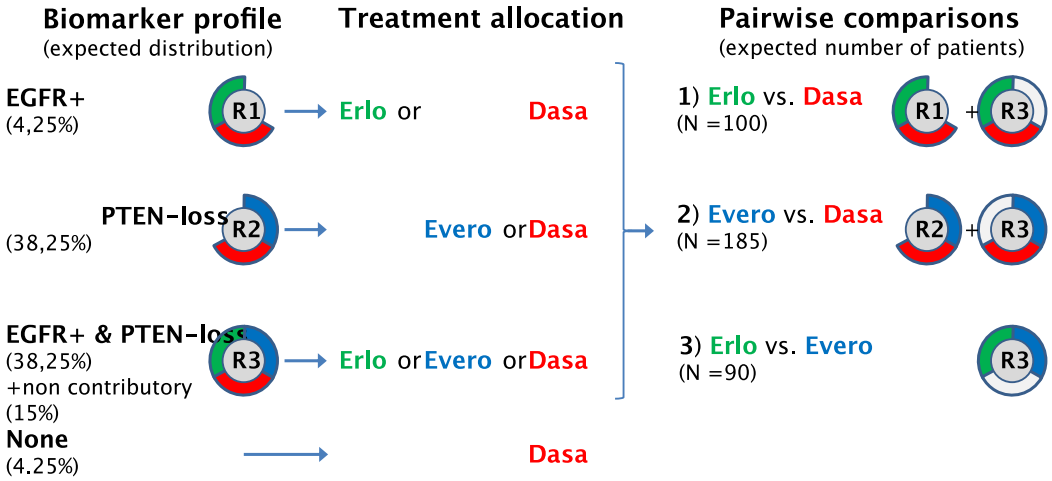

Extended Data Fig. 1 | Description of the 3 subtrials and the construction of the pairwise comparisons. Patients with EGFR-immunopositive tumors without PTEN loss of expression were randomized in R1 to receive either erlotinib or dasatinib. Patients with tumors showing PTEN loss only, without EGFR immunopositivity, were randomized in R2 to receive either everolimus or dasatinib. Patients with tumors exhibiting both EGFR immunopositivity and PTEN loss were randomized in R3 to receive one of the three drugs tested in the trial. Patients with an uninformative result for EGFR and/or PTEN were also randomized in R3 to receive one of the three drugs. Patients with tumors showing neither EGFR immunopositivity nor PTEN loss of expression were not randomized and received dasatinib. To maximize the number of patients in each comparison, pairwise comparisons were constructed by combining the subtrials. All patients enrolled in the R1 subtrial were included the erlotinib *versus* dasatinib comparison, together with patients from the R3 subtrial who were allocated to erlotinib or dasatinib. Similarly, all patients enrolled in the R2 subtrial were included in the everolimus *versus* dasatinib comparison, together with patients from the R3 subtrial, who were allocated to everolimus or dasatinib. Finally, patients enrolled in the R3 subtrial who were allocated to erlotinib or everolimus were included in the erlotinib *versus* everolimus comparison. Among the 95 patients initially randomized to receive everolimus, 92 ultimately patients received the drug, while 35 of the 36 patients randomized to erlotinib received this treatment.

https://doi.org/10.1038/s41591-026-04354-1

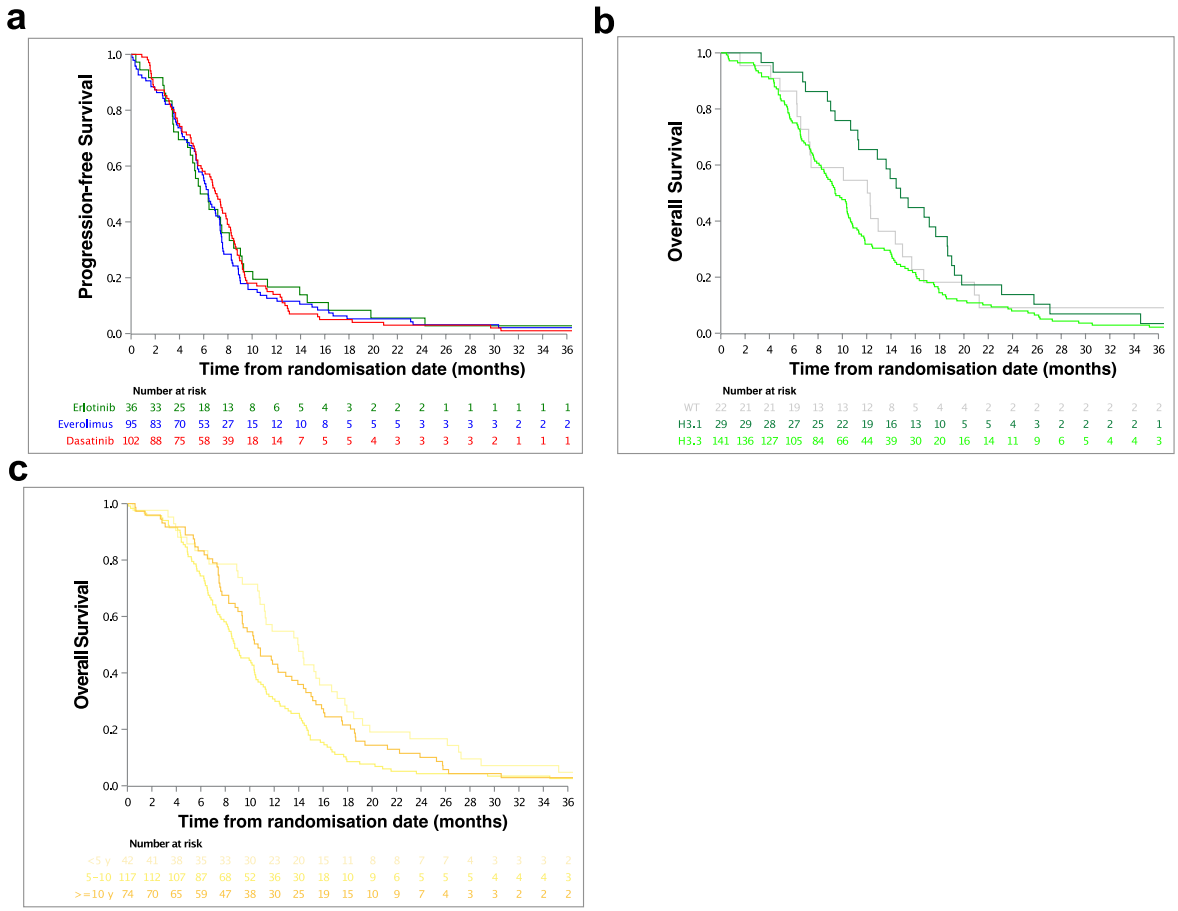

Extended Data Fig. 2 | Progression-Free Survival of the trial cohort according to treatment arm and overall survival according to predefined risk factors. **a**. Progression-Free Survival of the trial cohort according to the treatment arm (two-sided log-rank pvalue = 0.89). **b**. Overall Survival of the trial cohort according to the type of histone H3K27 alteration type (H3.3K27M, H3.1K27M and EZHIP over expression)(two-sided log-rank p-value = 0.064). **c**. Overall Survival of the trial cohort according to the age at diagnosis (two-sided log-rank p-value = 0.093).

https://doi.org/10.1038/s41591-026-04354-1

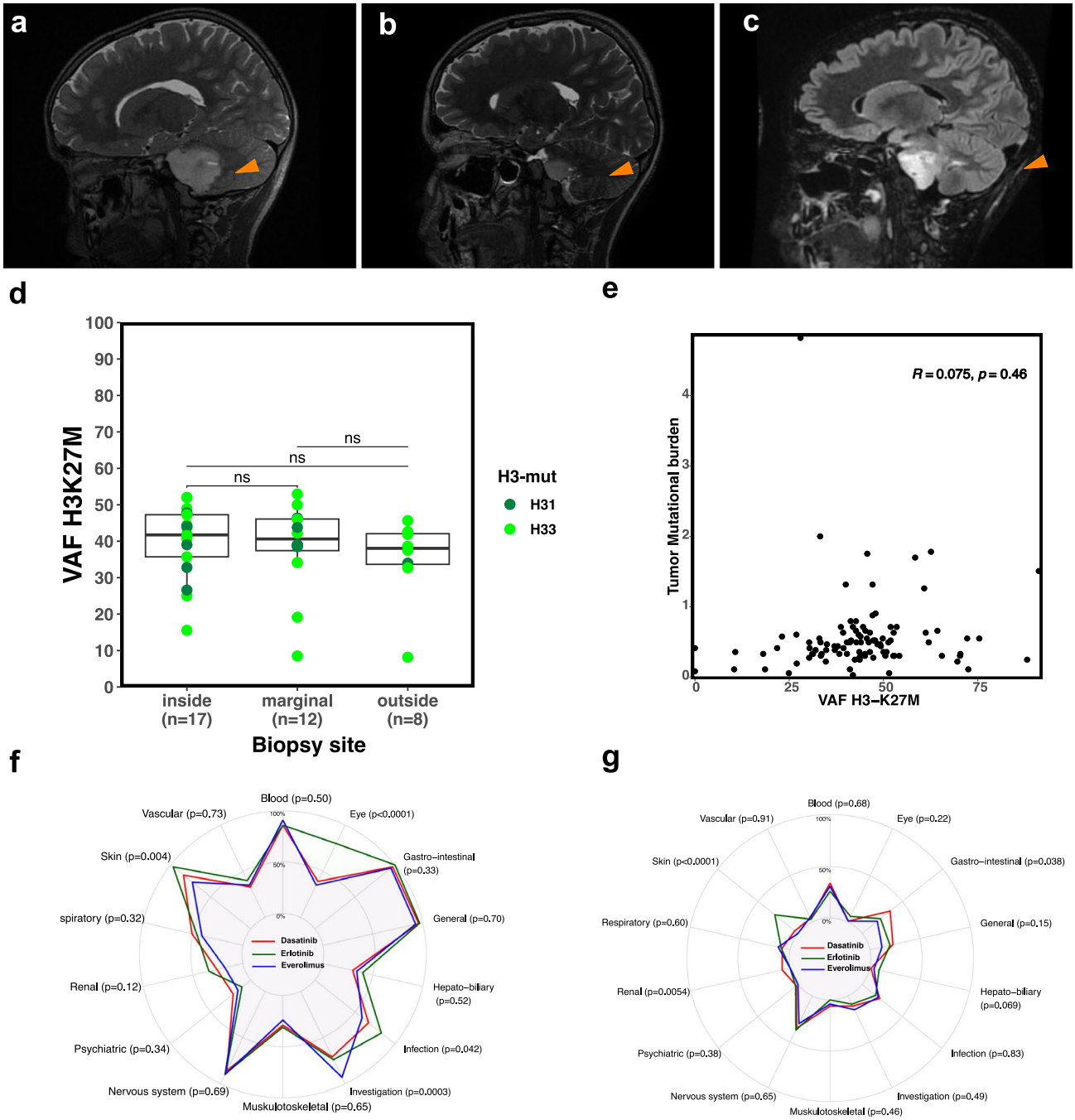

Extended Data Fig. 3 | Impact of biopsy location on tumor burden. **a-c**. Representative MRI images of biopsies performed inside (**a**), at the edge (**b**) and outside (**c**) the tumor, as indicated by orange arrows. **d**. Influence of biopsy site on tumor content estimated using the variant allele frequency (VAF) of the heterozygous H3K27M driver mutation in patients harboring *H3F3A* or *HIST1H3B* alterations, in the absence of copy number changes at the mutated histone locus (n = 39). Whiskers represent the minimum and maximum values within 1.5 × the interquartile range (IQR). Q1, Q2, and Q3 correspond to the 25th, 50th (median), and 75th percentiles, respectively. **e**. The Variant Allele Frequency of the H3K27M mutation is, on average, higher in 'inside tumor' biopsies, however, differences in distribution were not statistically significant (Kruskal-Wallis, $p = 0.42$). Relationship between sample tumor content and mutation load. **f**. Radar plot for all grade adverse events (AE) by system organ class (SOC). **g**. Radar plot for all severe adverse events (AE, grade > or = 3) by SOC.

https://doi.org/10.1038/s41591-026-04354-1

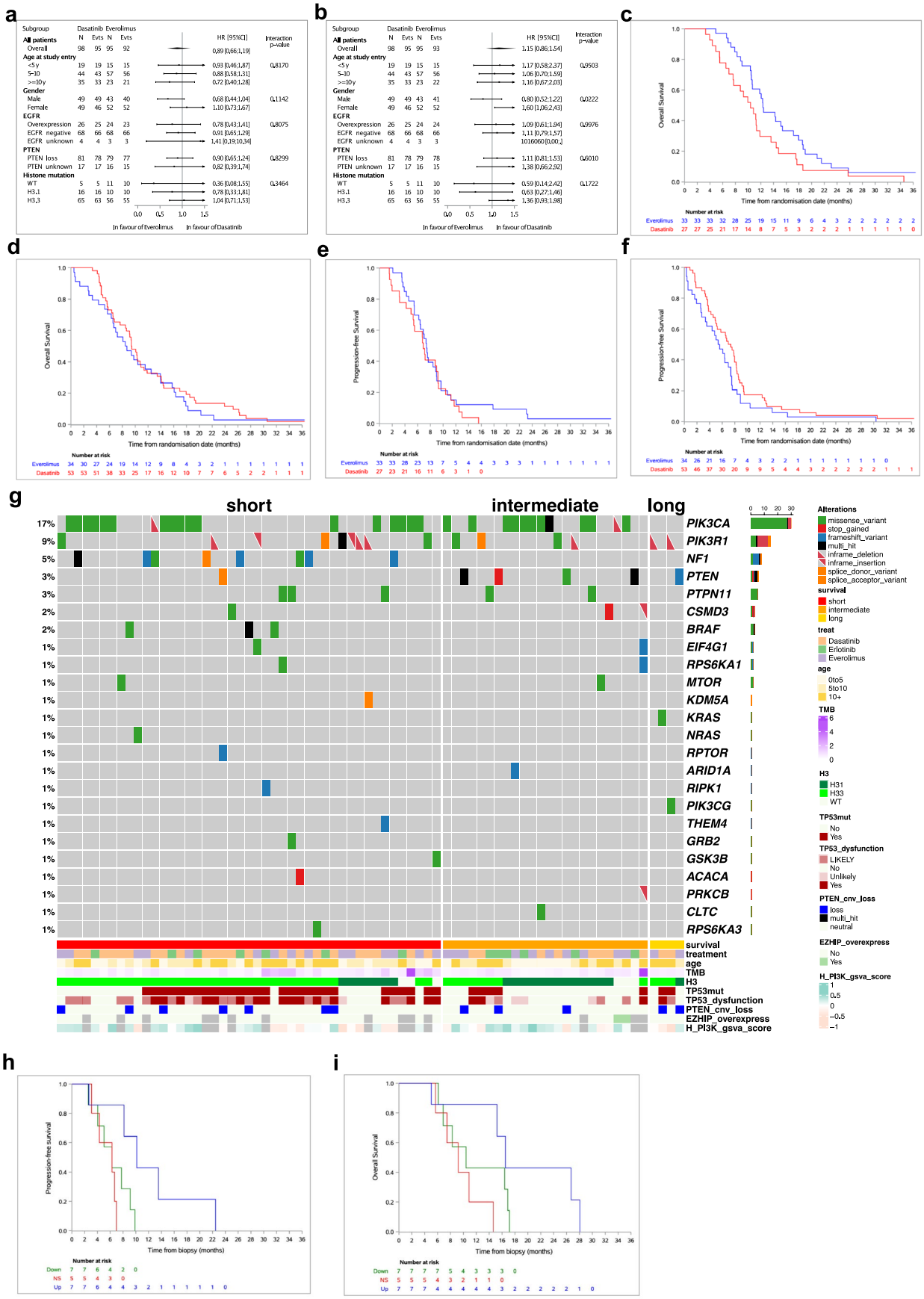

Extended Data Fig. 4 | See next page for caption.

https://doi.org/10.1038/s41591-026-04354-1

Extended Data Fig. 4 | Impact on survival of prespecified biomarkers, 1q chromosomal gain and PI3K/AKT/MTOR mutations. a-b. Forest plot for OS (**a**) and PFS (**b**) were computed for the largest pairwise comparison between everolimus and dasatinib, considering the following *a priori* risk factors : age, type of histone H3 mutation[7,22], biomarkers used for randomization, and gender. The diamond represents the overall treatment effect and its width the 95% confidence interval. Each horizontal line represents the hazard ratio (square) and its 95% confidence interval (CI) of treatment effect for each modality of a covariate. An arrow indicates that the upper limit of the 95% CI is outside the margins. The vertical line represents the null hypothesis of no treatment effect (hazard ratio = 1). c-d. Overall survival in patients with (**c**) or without (**d**) 1q gains, compared according to treatment with everolimus *vs*. dasatinib. e-f. Progression free survival in patients with (**e**) or without (**f**) 1q gains, compared according to treatment with everolimus *vs*. dasatinib treatment. **g**. Oncoplot presenting SNV alteration of genes involved in PI3K/AKT/MTOR pathway in DIPG ranked from the left to the right to a decreasing GSVA score of the pathway. On the right the SNV alteration of the patients without available RNAseq data are shown. **h-i**. To confirm the impact of theranostic biomarkers on the response to everolimus, we compiled an independent cohort of 19 patients with DIPG with available sequencing data, who were treated at Gustave Roussy with sirolimus or everolimus either before trial initiation or after randomization was stopped. Progression-free survival (H) and overall survival (I) were better in the patients with overexpression of the mTOR pathway.

https://doi.org/10.1038/s41591-026-04354-1

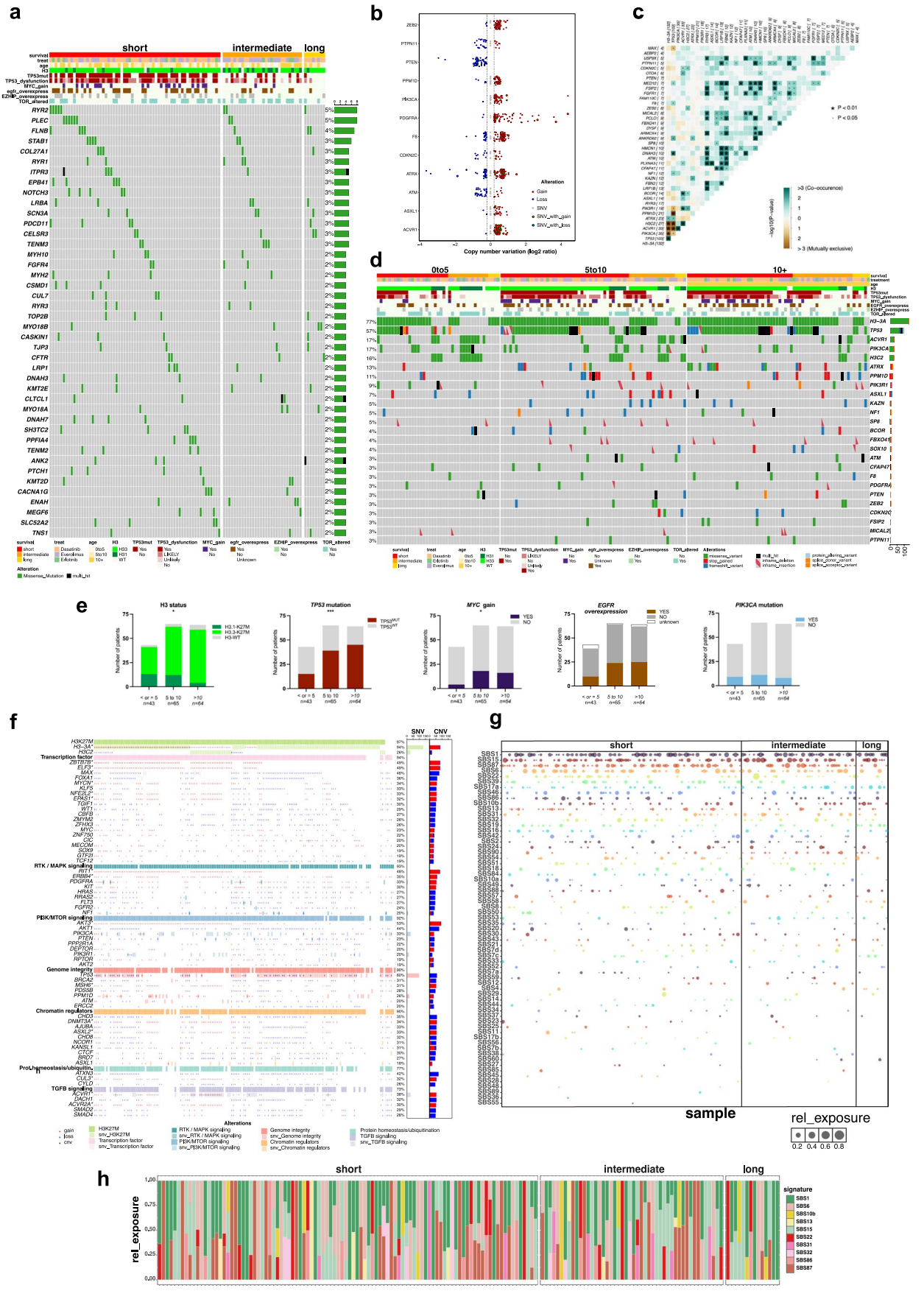

Extended Data Fig. 5 | See next page for caption.

https://doi.org/10.1038/s41591-026-04354-1

Extended Data Fig. 5 | Somatic/germline mutations and copy number variations classified according to survival classes or age at diagnosis. **a**- Oncoplot depicting the most frequently germline mutated genes in DIPG (n = 172), sorted in decreasing order of mutation frequency and stratified according to overall survival: below one year (short), between 1 and 2 year (intermediate) and above than 2 years (long). Forty-two mutated genes in at least 4 patients are shown, with mutation frequencies displayed as barplot on the right. Only germline SNVs predicted to be pathogenic, with more than 5 supporting reads and a VAF above 40% are displayed. A stacked barplot showing the number and types of variants per sample is shown on the right. **b**- CNVs of the mutated genes with the highest median VAF in Fig. 3b, shown on a log scale. Vertical lines indicate a 0.2 threshold. **c**-Mutual exclusivity analysis : two-sided pairwise Fisher's exact tests were performed for each of the 40 most frequently altered genes in DIPG. Log10-transformed pvalue are displayed using a blue-to-brown color scale, indicating co-occurrence and mutual exclusivity, respectively. * adjusted $p < 0.01$. adjusted $p < 0.05$. **d**- Oncoplot depicting the most frequently mutated genes in DIPG, sorted in decreasing order of mutation frequency and stratified according to age at diagnosis, presented similarly to Fig. 3a. **e**-Distributions of H3-K27, *TP53, PIK3CA* mutations, MYC gain and EGFR overexpression according to age at diagnosis are shown. Two-sided Fisher's exact test, $^{***}p < 0.001$, $^{*}p < 0.05$; *that is* $p = 0.02$ for H3 status, $p = 0.003$ for *TP53* mutation and $p = 0.07$ for MYC gain. **f**- Oncoprint showing an integrated annotation of somatic mutations and DNA copy number changes affecting selected pathways. Copy number gains and losses are indicated by small red and blue rectangles, respectively. When both gains and losses of a given gene are observed in the cohort, the rectangle is shown in black. On the right, bar-plots indicate the percentage of patients harboring SNVs or copy-number alterations at gene- or pathway-level. Genes located on chromosome 1q and chromosome 2 are marked with an asterisk, as these regions are frequently affected by CNAs. **g**- Comprehensive overview of COSMIC Single Base Substitution (SBS) signatures across the entire cohort, ordered by columns as in Fig. 3a. Signatures are ranked by decreasing recurrence in patients. **h**- Barplot showing, for each patient, the percentage of mutations belonging to each of the 15 more recurrent COSMIC SBS signatures in the entire cohort, ordered as in the oncoplot of Fig. 3a.

https://doi.org/10.1038/s41591-026-04354-1

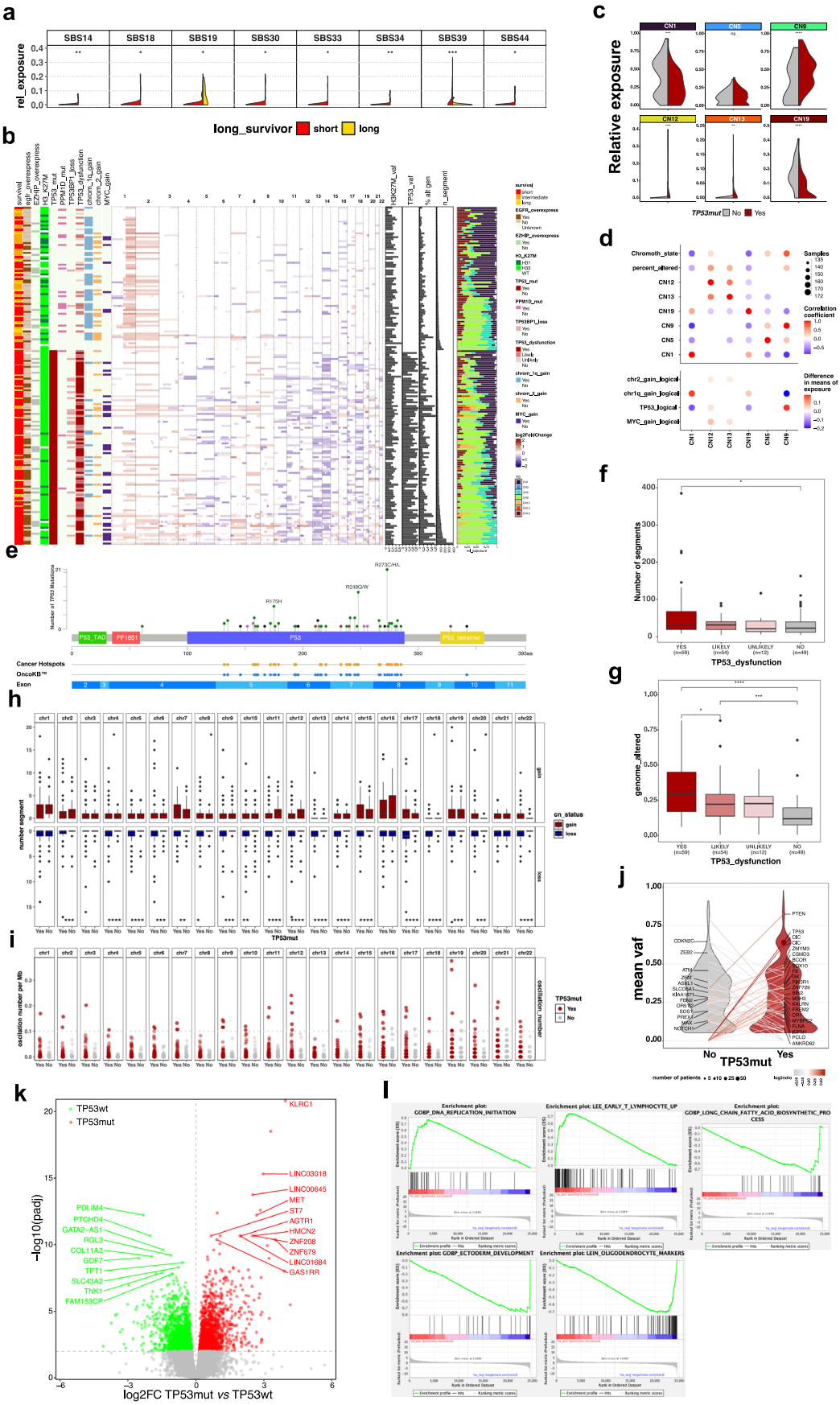

Extended Data Fig. 6 | See next page for caption.

https://doi.org/10.1038/s41591-026-04354-1

Extended Data Fig. 6 | Impact of TP53 alterations on gene expression and copy number variations. a-Violin plot showing SBS signatures significantly enriched in short- *versus* long-survival classes (two-sided t-test; *p < 0.05, **p < 0.01, ***p < 0.001) (L). SBS14 p = 0.008, SBS18 p = 0.019, SBS19 p = 0.040, SBS30 p = 0.023, SBS33 p = 0.038, SBS34 p = 0.008, SBS39 p = 0.0002, SBS44 p = 0.012. **b**- Heatmap of copy number genomic alterations (CNAs) in patients with DIPG profiled by WES. Red indicates gain and blue indicates losses, reflecting the log2 ratio of tumor *vs*. blood copy number values). Chromosomes are displayed as columns and samples as rows, stratified by $TP53^{MUT}$ and $TP53^{WT}$ tumor subgroups. Clinicopathological (EGFR overexpression by immunohistochemistry) and molecular annotations are shown as bars on the left. Coding SNVs with a VAF = or > to 5%, a minimum of 5 supporting reads and a frequency below 1% in the 1000 Genome database, as well as *TP53BP1* loss, are indicated. Histograms on the right show the VAF of H3-K27M, *TP53* mutations, the percentage of the genome affected by CNA, and the number of segments detected by CN analysis. A barplot displays, for each patient, the percentage of CNAs attributable to the 6 more recurrent COSMIC CNA signatures in the cohort. **c**-Violin plots comparing the percentage of CNAs attribuable to the 6 most prevalent COSMIC CN signatures in *TP53*-mutated and -wild-type tumors (two-sided t-test, **p < 0.01, *** p < 0.001, **** p < 0.0001). COSMIC copy-number signatures include CN1 Diploidy (p = 0.0003), CN5 Chromothripsis, CN9 Focal LOH – diploid and chromosomal instability (p = 2.1E-05), CN12 Focal LOH – chromosomal instability and 1X whole genome duplication (p = 0.0002), CN13 chromosomal LOH (p = 0.005); CN19 unknown aetiology (p = 7.2E-10). **d**- Associations between genome alteration signature exposures (or differences in exposure), and molecular features. Pearson correlation was used for exposure levels, and Kruskal-Wallis tests for differences in mean exposure, with false-discovery rate (FDR) P < 0.05 color-coded. Only molecular features significantly associated with CN signatures are shown, namely *TP53* mutation, chromosome 1q gain without chromosome 2 gain, the chromothripsis state. **e**- Lollipop plot of *TP53* alterations across the cohort, showing the distribution of variants along the amino acid sequence: missense (green, n = 88), truncating (black, n = 7), inframe (brown, n = 6), other variants (pink, n = 12). **f**- Box plots showing the distribution of the number of CNA segments detected by WES data according to the *TP53* dysfunction status. The value 'number of segments +1' is plotted on a log10 scale. Two-sided Wilcoxon test, *for $p < 0.05$, *that is* p = 0.016. **g**- Box plots showing the percentage of altered genome detected by WES data according to the *TP53* dysfunction status. The value 'number of segments +1' is plotted on a log10 scale. Two-sided Wilcoxon test, *, ***, **** for $p = 0.015$, p = 0.002 and p = 3.9E-07 respectively. **h**- Box plot showing the distribution of the number of segments per chromosome associated with gains or losses according to *TP53* mutational status. The value 'number of segments +1' is plotted on a log10 scale. Wilcoxon test, *, **, ***, **** for $p < 0.05$, 0.01, 0.001 and 0.00001 respectively. **i**- Dot blot showing chromothripsis scores per chromosome, calculated as the number of oscillations per Mb. **j**- Violin plots of the mutated genes whose VAF differ significantly between $TP53^{MUT}$ and $TP53^{WT}$ tumors. Only genes with a median VAF difference above 10 % between subgroups and mutated in at least 3 patients in one subgroup (VAF >5%) are shown. Median VAF per gene is indicated; dots are colored red when VAF is higher in $TP53^{MUT}$ tumors and gray otherwise. **k**- Volcano plot of differential gene expression comparing $TP53^{MUT}$ *versus* $TP53^{WT}$ tumors, displaying -log10 adjusted pvalue on y-axis and log2 fold change on the x-axis from DEseq2 analysis. Differentially Expressed genes in $TP53^{MUT}$ (n = 74) *versus* $TP53^{WT}$ (n = 64) with adjusted pvalue < 0.001 are color-coded in red or green. The 10 most upregulated and downregulated genes are labeled. **l**- GSEA plots showing enrichment of GOBP ectoderm development, GOBP DNA replication initiation, Lein oligodendrocyte markers, GOBP long chain fatty acid biosynthetic process, and Lee early T lymphocyte up pathways in $TP53^{MUT}$ *versus* $TP53^{WT}$ tumors.

https://doi.org/10.1038/s41591-026-04354-1

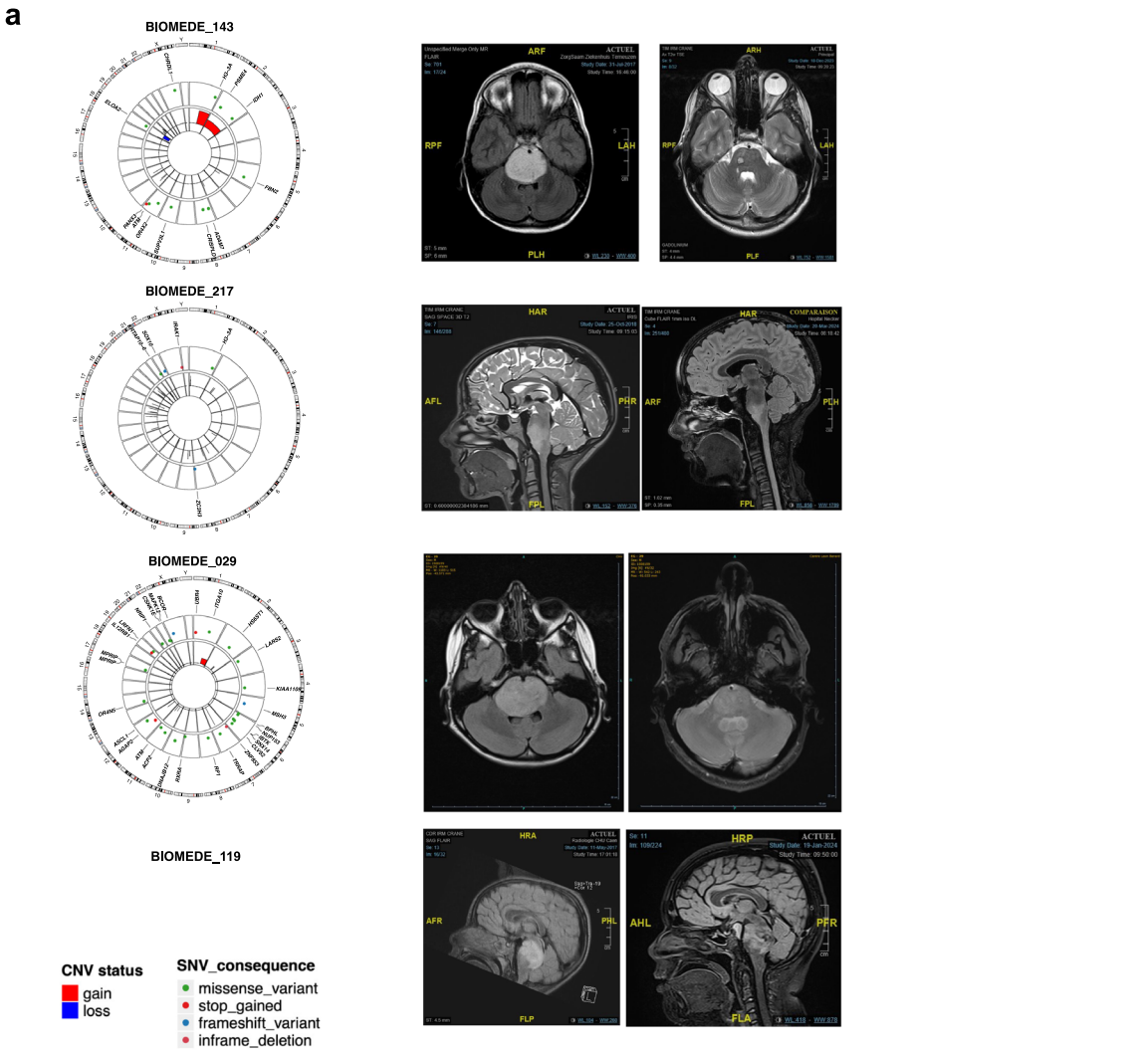

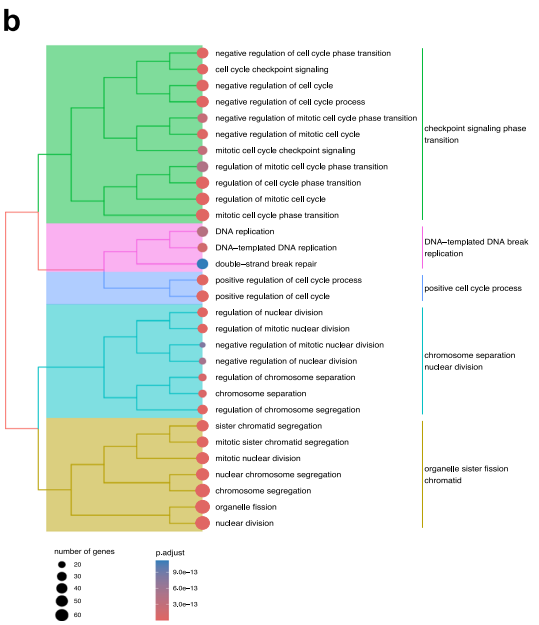

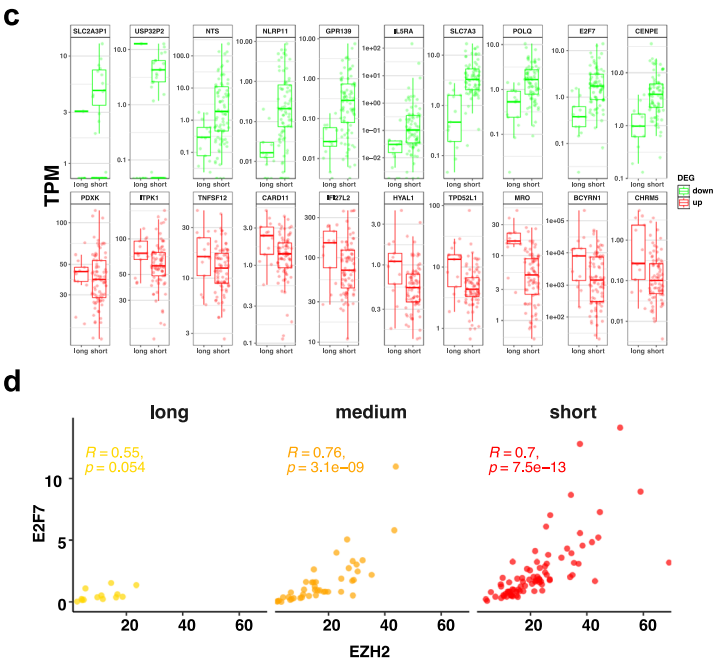

Extended Data Fig. 7 | See next page for caption.

https://doi.org/10.1038/s41591-026-04354-1

Extended Data Fig. 7 | Description of the long term survivors. a- Circos plot showing genome alterations in the 3 surviving patients on the left. The outer track color indicates SNVs, and the inner track show histograms of log2ratio values, reflecting gain (red) or loss (bleu) of genetic material associated with an absolute log2ratio > 0.20. Representative MRI sequences at diagnosis and follow-up of the four very long-term survivors on the right. BIOMEDE 143 : axial T2 FLAIR sequence at diagnosis and axial T2 sequence at follow-up showing complete disappearance of the tumor-related hypersignal and a decrease in brainstem size. The two T2 punctiform hypersignals correspond to the scar of the biopsy. BIOMEDE 217: sagital T2 sequence at diagnosis and sagittal T2 FLAIR sequence at last follow-up showing persistance of the hypersignal related to tumor infiltration although slightly decreased. BIOMEDE 029: axial T2 FLAIR sequence at diagnosis and axial T2 sequence at last follow-up showing a decrease in size of the brainstem and a partial reduction of the T2 hypersignal corresponding to the tumor infiltration. BIOMEDE 119: Sagittal T2 FLAIR sequence at diagnosis and at last follow-up showing the morphological changes in the tumor with the appearance of calcifications. Despite a slight increase in size, the neurological condition of the patients dis not deteriorate. **b.** Gene ontology tree derived from enrichment analysis on upregulated genes between long and short survivors. **c.** Box plot showing RNAseq expression levels (tpm) of the most strongly modulated genes in patients with a long (n = 13) *versus* short (n = 82) overall survival (adj p-value < 5.2E-09). Whiskers represent the minimum and maximum values within 1.5 × the interquartile range (IQR). Q1, Q2, and Q3 correspond to the 25th, 50th (median), and 75th percentiles, respectively. **d.** Expression level (tpm) of *E2F7* and *EZH2* in patients with DIPG with distinct overall survival (Spearman correlation).

https://doi.org/10.1038/s41591-026-04354-1

Extended Data Table 1 | Table of subtrial allocation according to biomarker profiles among the 233 patients meeting the general eligibility criteria

Biomarker status	EGFR overexpression	EGFR negative	EGFR unknown	Total
PTEN loss	R3 N=63 22 Erlo / 20 Ev / 21 D	R2 N=116 58 Ev / 58 D	R3 N=5 2 Erlo / 1 Ev / 2 D	N=184
PTEN positive (no PTEN loss)	R1 N=8 4 Erlo / 0 Ev / 4 D	No Randomisation	R1 N=0	N=8
PTEN unknown	R3 N=14 5 Erlo / 4 Ev / 5 D	R2 N=20 10 Ev / 10 D	R3 N=7 (1) 3 Erlo / 2 Ev / 2 D	N=41
Total	N=85	N=136	N=12	N=233

https://doi.org/10.1038/s41591-026-04354-1

Extended Data Table 2 | Table of subtrial allocation according to biomarker profiles among the 233 patients meeting the general eligibility criteria

	Estimates by treatment group			p
OS from randomisation (all randomized patients)	**Erlotinib N=36**	**Everolimus N=95**	**Dasatinib N=102**	
Median OS time (95%CI)	9.0 (7.4-14.4)	11.3 (10.3-13.4)	9.4 (8.2-10.8)	
2-year overall survival (SE)	8.7% (4.8%)	6.4% (2.5%)	10.0% (3.0%)	
OS from randomisation Erlotinib versus dasatinib	**Erlotinib N=36**		**Dasatinib N=34**	
Median OS time (95%CI)	9.0 mo (7.4-14.4)		8.5 mo (5.7-10.7)	
2-year overall survival (SE)	8.7% (4.8%)		6.1% (4.2%)	
Unstratified $HR_{erlo\ vs\ dasa}$ (95%CI)	0.69 (0.42-1.13)		1 (ref)	0.14
Stratified $HR_{erlo\ vs\ dasa}$[2] (95%CI)	0.87 (0.52-1.46)		1 (ref)	0.59
OS from randomisation Everolimus versus dasatinib		**Everolimus N=95**	**Dasatinib N=98**	
Median OS time (95%CI)		11.3 mo (10.3-13.4)	9.4 mo (8.2-10.8)	
2-year overall survival (SE)		6.4% (2.5%)	10.4% (3.2%)	
Unstratified $HR_{evero\ vs\ dasa}$ (95%CI)		0.86 (0.64-1.14)	1 (ref)	0.29
Stratified $HR_{evero\ vs\ dasa}$[3] (95%CI)		0.89 (0.66-1.19)	1 (ref)	0.42
OS from randomisation Erlotinib versus everolimus	**Erlotinib N=32**	**Everolimus N=27**		
Median OS time (95%CI)	10.2 mo (7.3-14.8)	10.5 mo (7.3-11.8)		
2-year overall survival (SE)	9.8% (5.4%)	3.9% (3.8%)		
Unstratified $HR_{erlo\ vs\ evero}$ (95%CI)	0.79 (0.46-1.34)	1 (ref)		0.39
Stratified $HR_{erlo\ vs\ evero}$[4] (95%CI)	0.94 (0.54-1.65)	1 (ref)		0.84
OS from date of biopsy among patients who started study treatment*	**Erlotinib N=35***	**Everolimus N=92***	**Dasatinib N=102**	
Median OS time (95%CI)	9.7 mo (7.8-14.6)	11.9 mo (10.7-14.2)	9.9 mo (8.8-11.2)	
2-year overall survival (SE)	8.9% (4.9%)	7.7% (2.8%)	11.0% (3.1%)	
P-value of the comparison to historical data	0.75	0.95	0.22	
OS from radiological diagnosis among patients who started study treatment*	**Erlotinib N=35***	**Everolimus N=92***	**Dasatinib N=102**	
Median OS time (95%CI)	10.3 (8.0-14.8)	12.1 mo (10.9-14.6)	10.5 mo (9.5-11.5)	
2-year overall survival (SE)	9.1% (5%)	10.0% (3.1%)	11.0% (3.1%)	

https://doi.org/10.1038/s41591-026-04354-1

Extended Data Table 3 | Table of subtrial allocation according to biomarker profiles among the 233 patients meeting the general eligibility criteria

System Organ Class / Preferred Term	Erlotinib (N= 35)				Everolimus (N= 91)				Dasatinib (N= 101)				Comparison between the 3 arms	
	Gr >=1		Gr >=3		Gr >=1		Gr >=3		Gr >=1		Gr >=3		Gr >=1	Gr >=3
	N	%	N	%	N	%	N	%	N	%	N	%	p-value	p-value
Any type	35	100	29	83	91	100	69	76	100	99	80	79	1.00	0.67
Blood and lymphatic system disorders	30	86	9	26	83	91	28	31	87	86	34	34	0.5	0.68
Cardiac disorders	3	9	0	0	4	4	0	0	2	2	0	0	0.18	NA
Ear and labyrinth disorders	3	9	0	0	10	11	0	0	15	15	0	0	0.55	NA
Endocrine disorders	2	6	0	0	9	10	0	0	10	10	0	0	0.73	NA
Eye disorders	28	80	2	6	32	35	1	1	39	39	1	1	<0.0001	0.22
Gastrointestinal disorders	35	##	8	23	86	95	17	19	98	97	35	35	0.33	0.038
General disorders and administration site conditions	34	97	7	20	85	93	11	12	97	96	23	23	0.70	0.15
Hepatobiliary disorders	14	40	3	9	31	34	4	4	30	30	1	1	0.52	0.069
Immune system disorders	0	0	0	0	1	1	1	1	1	1	0	0	1.0	0.56
Infections and infestations	29	83	6	17	54	59	18	20	68	67	22	22	0.042	0.83
Injury, poisoning and procedural complications	0	0	0	0	2	2	1	1	3	3	1	1	0.85	1.0
Investigations / Metabolism and nutrition disorders	26	74	3	9	85	93	14	15	72	71	11	11	0.0003	0.49
Musculoskeletal and connective tissue disorders	11	31	0	0	22	24	4	4	29	29	6	6	0.65	0.46
Nervous system disorders	31	89	13	37	82	90	27	30	87	86	35	35	0.69	0.65
Psychiatric disorders	4	11	1	3	15	16	0	0	22	22	2	2	0.34	0.38
Renal and urinary disorders	12	34	0	0	16	18	0	0	26	26	8	8	0.12	0.0054
Reproductive system and breast disorders	0	0	0	0	3	3	0	0	4	4	1	1	0.77	1.0
Respiratory, thoracic and mediastinal disorders	16	46	3	9	37	41	11	12	52	51	8	8	0.32	0.60
Skin and subcutaneous tissue disorders	34	97	10	29	66	73	0	0	85	84	4	4	0.004	<0.0001
Vascular disorders	14	40	1	3	32	35	5	5	33	33	4	4	0.73	0.91

nature portfolio

Corresponding author(s): Marie-Anne Debily, Jacques Grill

Last updated by author(s): Mar 13, 2023

Reporting Summary

Nature Portfolio wishes to improve the reproducibility of the work that we publish. This form provides structure for consistency and transparency in reporting. For further information on Nature Portfolio policies, see our Editorial Policies and the Editorial Policy Checklist.

Statistics

For all statistical analyses, confirm that the following items are present in the figure legend, table legend, main text, or Methods section.

n/a	Confirmed	
☐	☒	The exact sample size (*n*) for each experimental group/condition, given as a discrete number and unit of measurement
☐	☒	A statement on whether measurements were taken from distinct samples or whether the same sample was measured repeatedly
☐	☒	The statistical test(s) used AND whether they are one- or two-sided *Only common tests should be described solely by name; describe more complex techniques in the Methods section.*
☐	☒	A description of all covariates tested
☐	☐	A description of any assumptions or corrections, such as tests of normality and adjustment for multiple comparisons
☐	☒	A full description of the statistical parameters including central tendency (e.g. means) or other basic estimates (e.g. regression coefficient) AND variation (e.g. standard deviation) or associated estimates of uncertainty (e.g. confidence intervals)
☐	☒	For null hypothesis testing, the test statistic (e.g. *F*, *t*, *r*) with confidence intervals, effect sizes, degrees of freedom and *P* value noted *Give P values as exact values whenever suitable.*
☒	☐	For Bayesian analysis, information on the choice of priors and Markov chain Monte Carlo settings
☒	☐	For hierarchical and complex designs, identification of the appropriate level for tests and full reporting of outcomes
☐	☒	Estimates of effect sizes (e.g. Cohen's *d*, Pearson's *r*), indicating how they were calculated

Our web collection on statistics for biologists contains articles on many of the points above.

Software and code

Policy information about availability of computer code

Data collection	*Provide a description of all commercial, open source and custom code used to collect the data in this study, specifying the version used OR state that no software was used.*
Data analysis	*Provide a description of all commercial, open source and custom code used to analyse the data in this study, specifying the version used OR state that no software was used.*

For manuscripts utilizing custom algorithms or software that are central to the research but not yet described in published literature, software must be made available to editors and reviewers. We strongly encourage code deposition in a community repository (e.g. GitHub). See the Nature Portfolio guidelines for submitting code & software for further information.

Data

Policy information about availability of data

All manuscripts must include a data availability statement. This statement should provide the following information, where applicable:

- Accession codes, unique identifiers, or web links for publicly available datasets
- A description of any restrictions on data availability
- For clinical datasets or third party data, please ensure that the statement adheres to our policy

Done page 60
DATA AVAILABILITY STATEMENT

The analyses reported in this paper are based on a data cutoff of 2022, except for LTS data, which were updated in September 2025extended. Genomic data are available through the European Genome-Phenome Archive (EGAS50000001164). The list of variables in the trial database can be obtained upon request. Clinical data (sex, age, overall survival, progression-free survival) will be available upon request through the signature of a DTA since these data are sensitive and belong to the sponsor of the study. Radiologic data, including diagnosis and follow-up imaging are currently being uploaded and stored to an imaging repository at The Centre pour l'Acquisition et le Traitement des Images - CATI - (Neurospin data center in the CEA Paris-Saclay). As studies are still ongoing on the clinical and radiological data and as these data are not necessary to interpret the study, these data will become publicly available later. Meanwhile, they will be accessible upon request provided the proposed study is not in competion with current project of the consortium. All these data will be available upon request from the corresponding authors.

Research involving human participants, their data, or biological material

Policy information about studies with human participants or human data. See also policy information about sex, gender (identity/presentation), and sexual orientation and race, ethnicity and racism.

Reporting on sex and gender	yes for the treatment effect
Reporting on race, ethnicity, or other socially relevant groupings	French legislation does not allow clinical study to collect ethnicity.
Population characteristics	described in the manuscript, lines 1090-1105
Recruitment	described in the manuscript, lines 1090-1105
Ethics oversight	described in the manuscript, lines 1197-1200

Note that full information on the approval of the study protocol must also be provided in the manuscript.

Field-specific reporting

Please select the one below that is the best fit for your research. If you are not sure, read the appropriate sections before making your selection.

☒ Life sciences ☐ Behavioural & social sciences ☐ Ecological, evolutionary & environmental sciences

For a reference copy of the document with all sections, see nature.com/documents/nr-reporting-summary-flat.pdf

Life sciences study design

All studies must disclose on these points even when the disclosure is negative.

Sample size	described in the manuscript, pages 50-51
Data exclusions	not applicable
Replication	not applicable
Randomization	described in the manuscript, lines 1202-1218
Blinding	not applicable

Reporting for specific materials, systems and methods

We require information from authors about some types of materials, experimental systems and methods used in many studies. Here, indicate whether each material, system or method listed is relevant to your study. If you are not sure if a list item applies to your research, read the appropriate section before selecting a response.

Materials & experimental systems

n/a	Involved in the study
☐	☒ Antibodies
☒	☐ Eukaryotic cell lines
☒	☐ Palaeontology and archaeology
☒	☐ Animals and other organisms
☐	☒ Clinical data
☒	☐ Dual use research of concern
☒	☐ Plants

Methods

n/a	Involved in the study
☒	☐ ChIP-seq
☒	☐ Flow cytometry
☒	☐ MRI-based neuroimaging

Antibodies

Antibodies used: described in the manuscript, lines 1309-1323

Validation: not applicable

Clinical data

Policy information about clinical studies

All manuscripts should comply with the ICMJE guidelines for publication of clinical research and a completed CONSORT checklist must be included with all submissions.

Clinical trial registration: NCT02233049

Study protocol: provided as an annex

Data collection: described in the manuscript lines 1248-1306

Outcomes: described in the manuscript lines 1248-1306

Plants

Seed stocks: *Report on the source of all seed stocks or other plant material used. If applicable, state the seed stock centre and catalogue number. If plant specimens were collected from the field, describe the collection location, date and sampling procedures.*

Novel plant genotypes: *Describe the methods by which all novel plant genotypes were produced. This includes those generated by transgenic approaches, gene editing, chemical/radiation-based mutagenesis and hybridization. For transgenic lines, describe the transformation method, the number of independent lines analyzed and the generation upon which experiments were performed. For gene-edited lines, describe the editor used, the endogenous sequence targeted for editing, the targeting guide RNA sequence (if applicable) and how the editor was applied.*

Authentication: *Describe any authentication procedures for each seed stock used or novel genotype generated. Describe any experiments used to assess the effect of a mutation and, where applicable, how potential secondary effects (e.g. second site T-DNA insertions, mosiacism, off-target gene editing) were examined.*